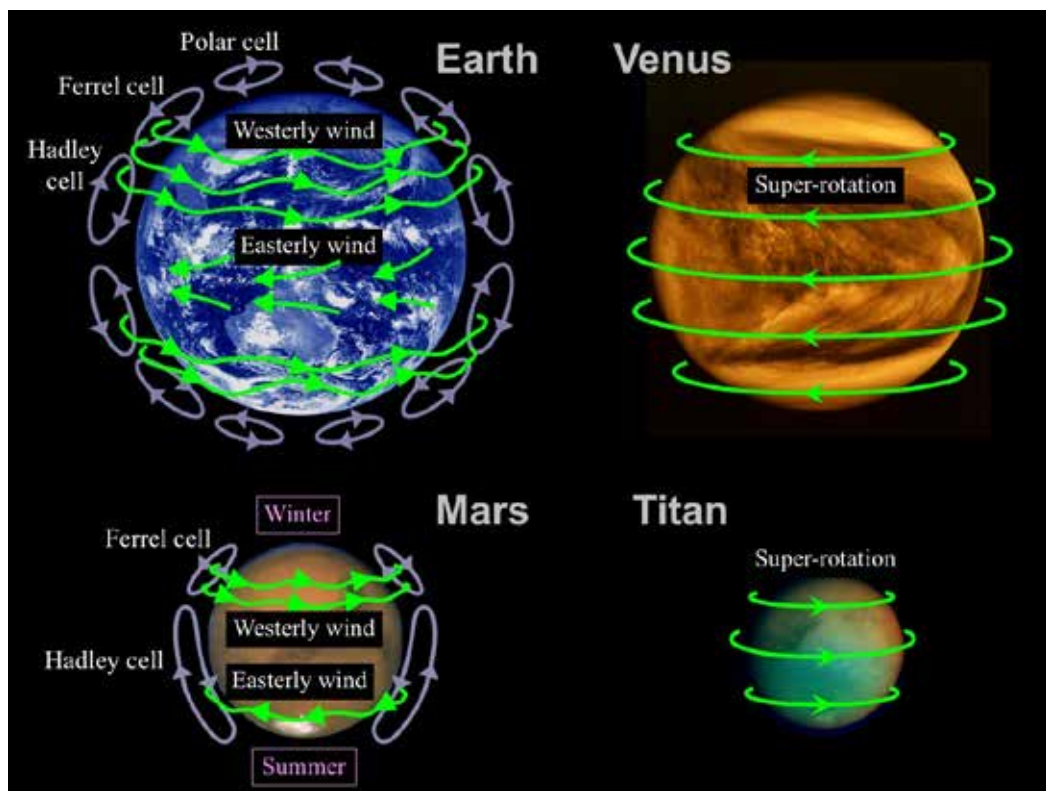
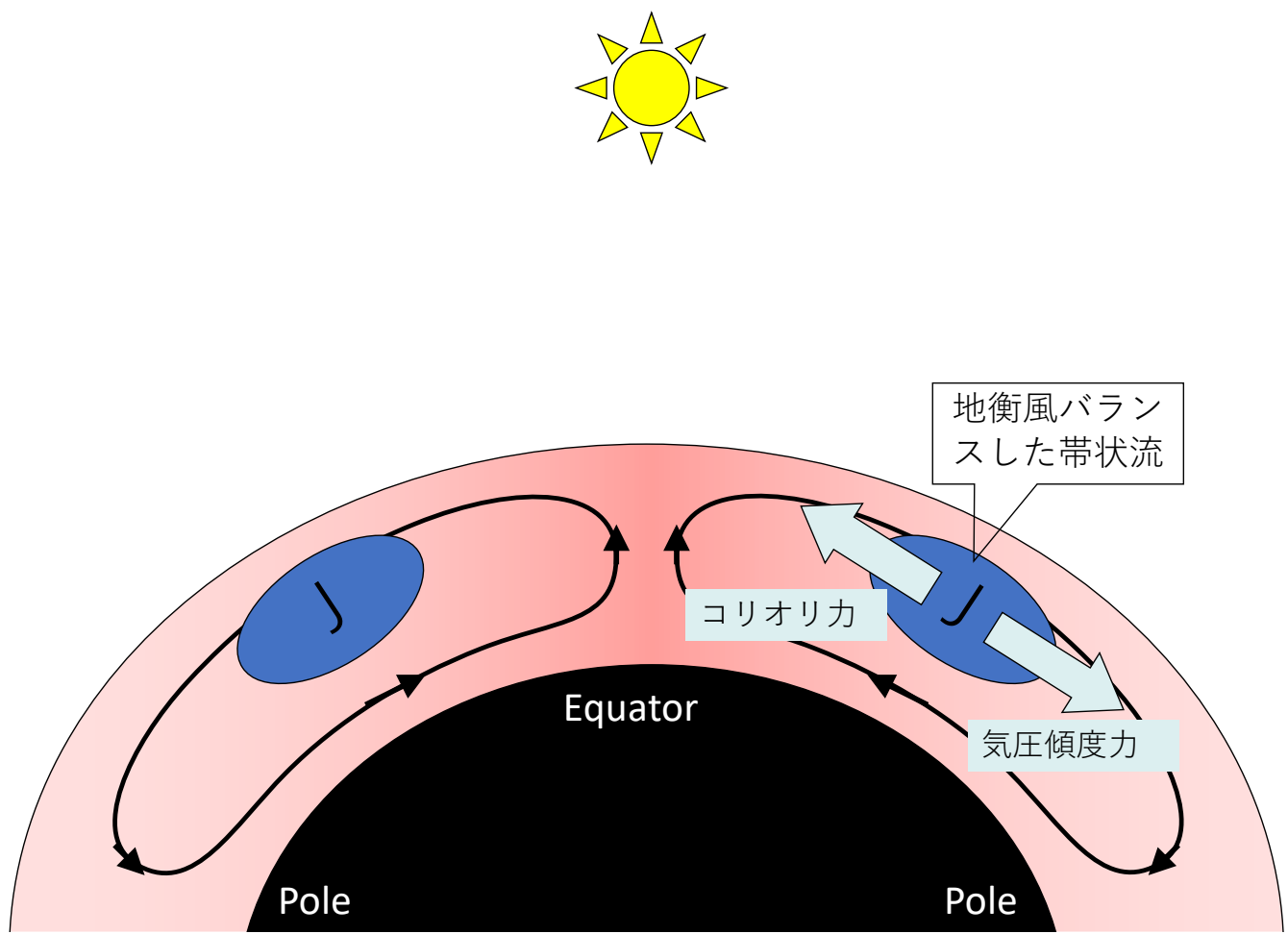
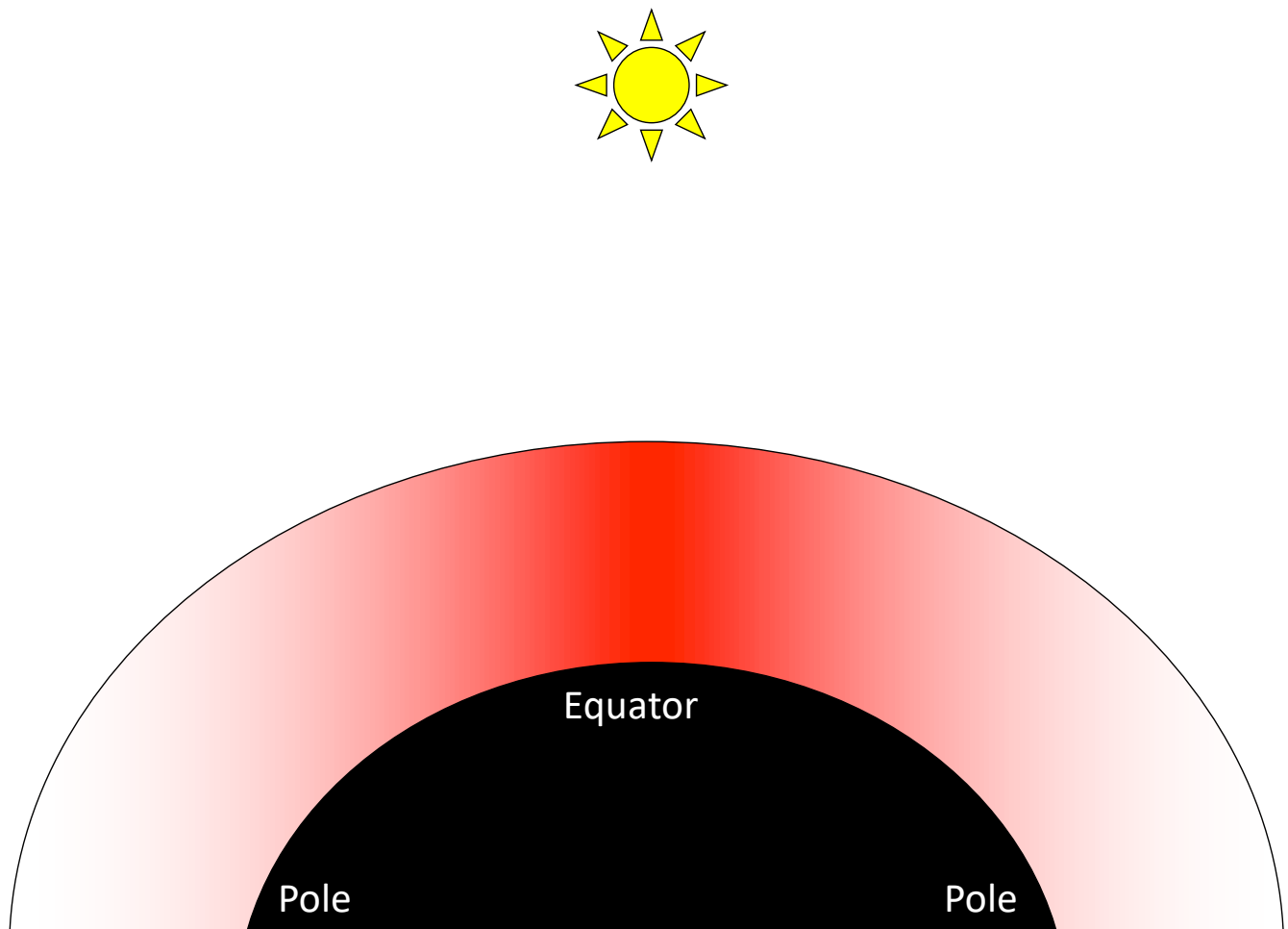


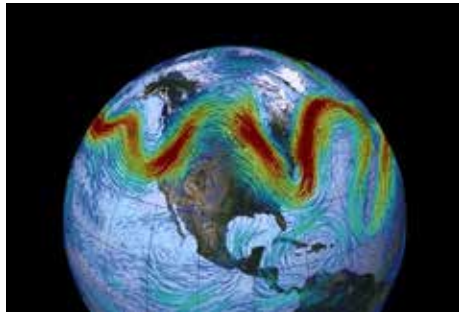
# Atmospheric dynamics II

## Planetary-scale atmospheric circulation





# Baroclinic wave disturbance



Frontal dust storms on Mars (Wang et al. 2005)

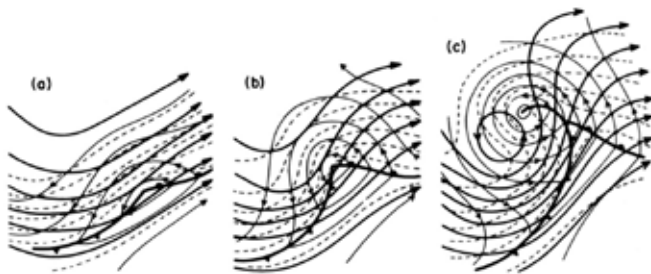


**Fig. 6.5** Schematic 500-hPa contours (heavy solid lines), 1000-hPa contours (thin lines), and 1000–500 hPa thickness (dashed) for a developing baroclinic wave at three stages of development. (After Palmén and Newton, 1969.)

Holton 2012

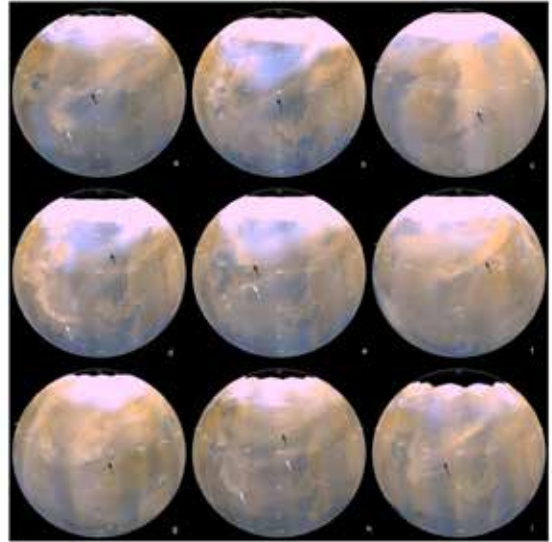


**Figure 5.** Examples of flanking dust storms in different channels, seasons, and years. Each panel is a Mars daily global map projected onto a sphere with local arrows pointing to the direction of the front. The panels from top to the bottom are for MGS-mosaic Years 1 (1999–2001), 2 (2001–2003), and 3 (2003–2005), respectively. Figures 5a, 5b, 5d, 5e, 5h, and 5i are for the Acidalia channel; Figure 5c is for the Arabia channel; Figures 5f and 5g are for the Utopia channel. The  $\lambda_s$  values are (a)  $210^\circ$ , (b)  $714^\circ$ , (c)  $334^\circ$ , (d)  $316^\circ$ , (e)  $324^\circ$ , (f)  $324^\circ$ , (g)  $207^\circ$ , (h)  $214^\circ$ , and (i)  $236^\circ$ .

## Quasi-geostrophic vorticity equation

$$\frac{\partial \zeta_g}{\partial t} = -\vec{v}_g \cdot \nabla(\zeta_g + f) + f_0 \frac{\partial \omega}{\partial p}$$

$\nabla$  : horizontal differentiation

$$\zeta_g \equiv \frac{\partial v_g}{\partial x} - \frac{\partial u_g}{\partial y} = \frac{\nabla^2 \Phi'}{f_0} \quad : \text{geostrophic vorticity}$$

$$\vec{v}_g \equiv \frac{1}{f_0} \vec{k} \times \nabla \Phi \quad : \text{geostrophic wind}$$

$\Phi$  : geopotential

$f$  : Coriolis parameter (planetary vorticity)

$\omega \equiv dp/dt$  : vertical velocity in pressure coordinate

# Equation of thermodynamics

$$\left( \frac{\partial}{\partial t} + \vec{v}_g \cdot \nabla \right) \frac{\partial \Phi'}{\partial p} + \sigma \omega = 0$$

$$\Phi(x, y, p, t) = \bar{\Phi}(p) + \Phi'(x, y, p, t) \quad : \text{geopotential}$$

$$\sigma \equiv -\frac{1}{\bar{\rho}\bar{\theta}} \frac{\partial \bar{\theta}}{\partial p} = \frac{1}{p} \frac{d}{dp} \left( p \frac{d\bar{\Phi}}{dp} - \frac{R}{c_p} \bar{\Phi} \right) \quad : \text{(static stability)}$$

$$\frac{\partial \bar{\Phi}}{\partial p} / \partial p = -R\bar{T}/p \quad : \text{(temperature)}$$

$$\frac{\partial \Phi'}{\partial p} / \partial p = -RT'/p \quad : \text{(temperature)}$$

# Omega equation

Combining the vorticity equation and the thermodynamics equation to eliminate the time derivative term, we get the “omega equation”:

$$\underbrace{\left( \nabla^2 + \frac{f_0^2}{\sigma} \frac{\partial^2}{\partial p^2} \right) \omega}_{(A)} = \frac{f_0}{\sigma} \frac{\partial}{\partial p} \left[ \vec{v}_g \cdot \nabla (\zeta_g + f) \right] + \frac{f_0 R}{\sigma p} \left[ \nabla^2 (\vec{v}_g \cdot \nabla T) \right]$$

Let us consider a sinusoidal perturbation

$$\omega \propto \sin(\pi p/p_s) \sin(kx) \cos(ly)$$

Then the term (A) becomes

$$\left( \nabla^2 + \frac{f_0^2}{\sigma} \frac{\partial^2}{\partial p^2} \right) \omega \approx - \left[ k^2 + l^2 + \frac{1}{\sigma} \left( \frac{f_0 \pi}{p_0} \right)^2 \right] \omega$$

Since the sign of the vertical velocity  $w$  is opposite to that of  $\omega$  ( $w \approx -\omega$ ), (A) is proportional to the vertical velocity. (Upward motion is forced where the right-hand side is positive and downward motion is forced where it is negative.)

# Vertical motion forced by the advection of vorticity

Omega equation

$$\left( \nabla^2 + \frac{f_0^2}{\sigma} \frac{\partial^2}{\partial p^2} \right) \omega = \frac{f_0}{\sigma} \frac{\partial}{\partial p} \left[ \vec{v}_g \cdot \nabla (\zeta_g + f) \right] + \frac{f_0 R}{\sigma p} \left[ \nabla^2 (\vec{v}_g \cdot \nabla T) \right]$$

$$\approx w \quad (B)$$

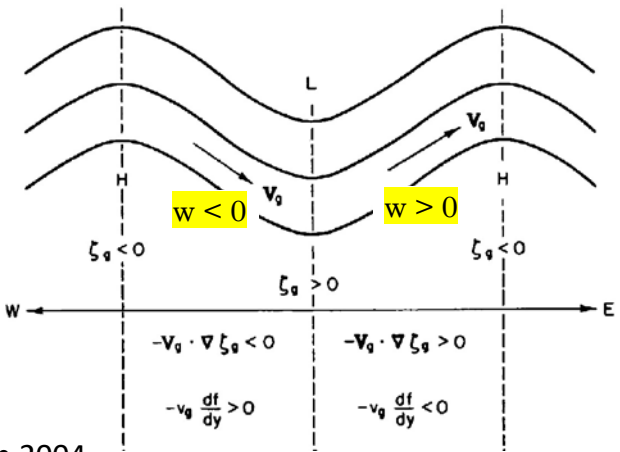
The term (B) is rewritten as

$$(B) \propto \frac{\partial}{\partial z} \left( -\vec{v}_g \cdot \nabla \zeta_g - v_g \frac{\partial f}{\partial y} \right)$$

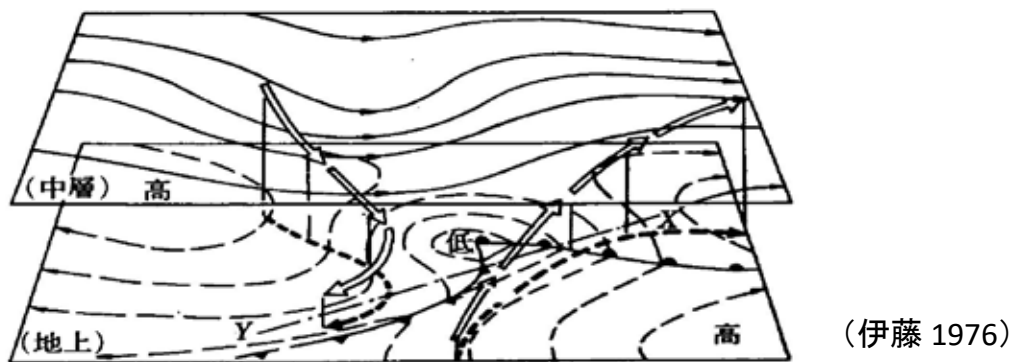
For a short-wave system where relative vorticity advection is larger than the planetary vorticity advection, the pattern of vertical motion forced by the advection of vorticity by the thermal wind has

$w < 0$  : west of trough

$w > 0$  : east of trough



## 3D structure of baroclinic wave disturbance



cold advection below trough → development of trough  
warm advection below ridge → development of ridge

rising warm air to the east of trough & subsidence of cold air to the west of trough  
→ conversion from eddy potential energy to eddy kinetic energy

# Meridional transport

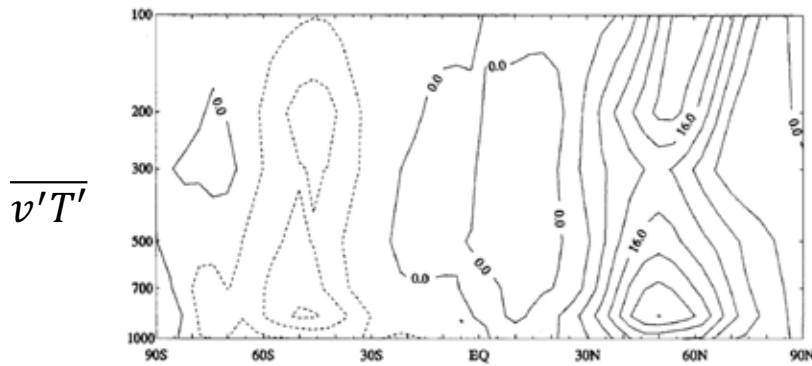
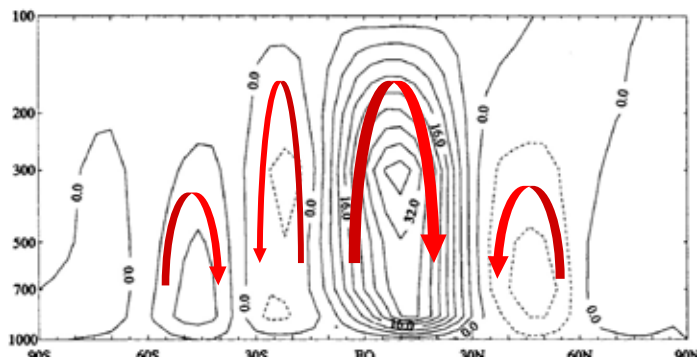


Fig. 10.3 Observed northward eddy heat flux distribution ( $^{\circ}\text{C m s}^{-1}$ ) for Northern Hemisphere winter.  
(Adapted from Schubert et al., 1990.)

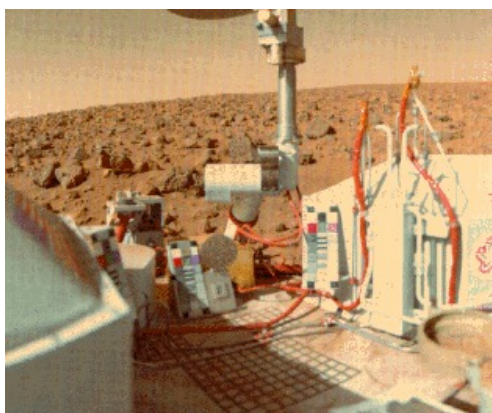
stream  
function



Holton 2004

Fig. 10.7 Streamfunction (units:  $10^2 \text{ kg m}^{-1} \text{s}^{-1}$ ) for the observed Eulerian mean meridional circulation for Northern Hemisphere winter, based on the data of Schubert et al. (1990).

## Surface meteorological measurements on Mars by Viking-2



(Barnes, 1980)

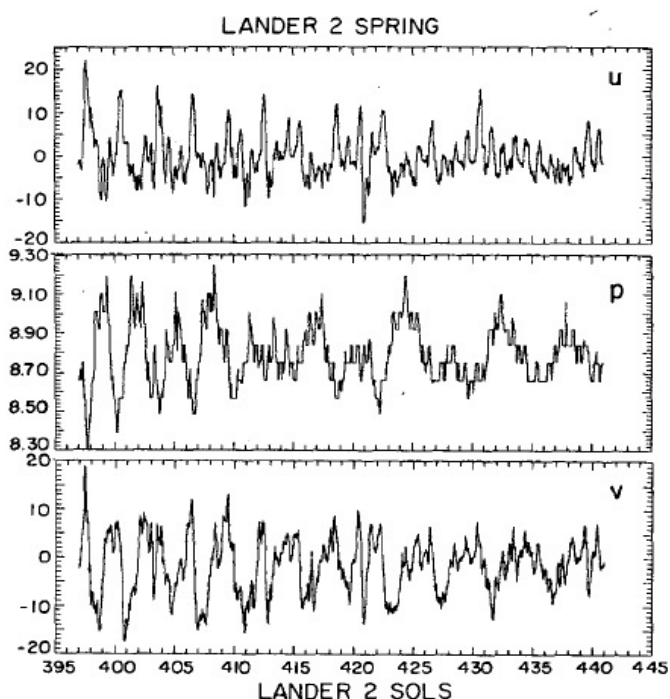
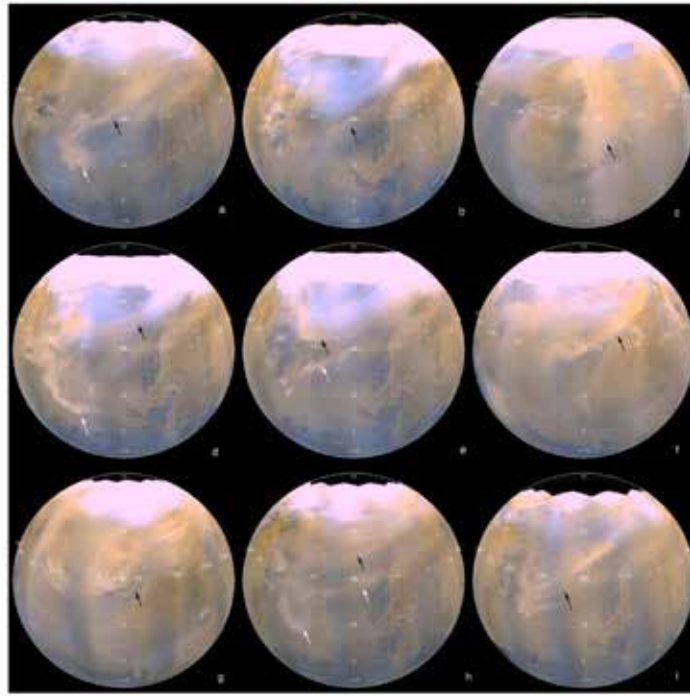


FIG. 2. The unfiltered pressure and zonal ( $u$ ) and meridional ( $v$ ) wind data for a 44-sol portion of the spring period at Lander 2. The pressure is in mb, with the wind speeds in  $\text{m s}^{-1}$ .

## Frontal dust storms on Mars (Wang et al. 2005)



**Figure 5.** Examples of flushing dust storms in different channels, seasons, and years. Each panel is a Mars daily global map projected onto a sphere with black arrows pointing to the main frontal features. The three rows from the top to the bottom are for MGS mapping Years 1 (1999–2001), 2 (2001–2003), and 3 (2003–2005), respectively. Figures 5a, 5b, 5d, 5e, 5h, and 5i are for the Acidalia channel. Figure 5c is for the Arcadia channel. Figures 5f and 5g are for the Utopia channel. The  $I_S$  values are (a) 210°, (b) 314°, (c) 336°, (d) 316°, (e) 324°, (f) 324°, (g) 207°, (h) 214°, and (i) 230°.

## Meridional circulation in a Martian GCM (general circulation model)

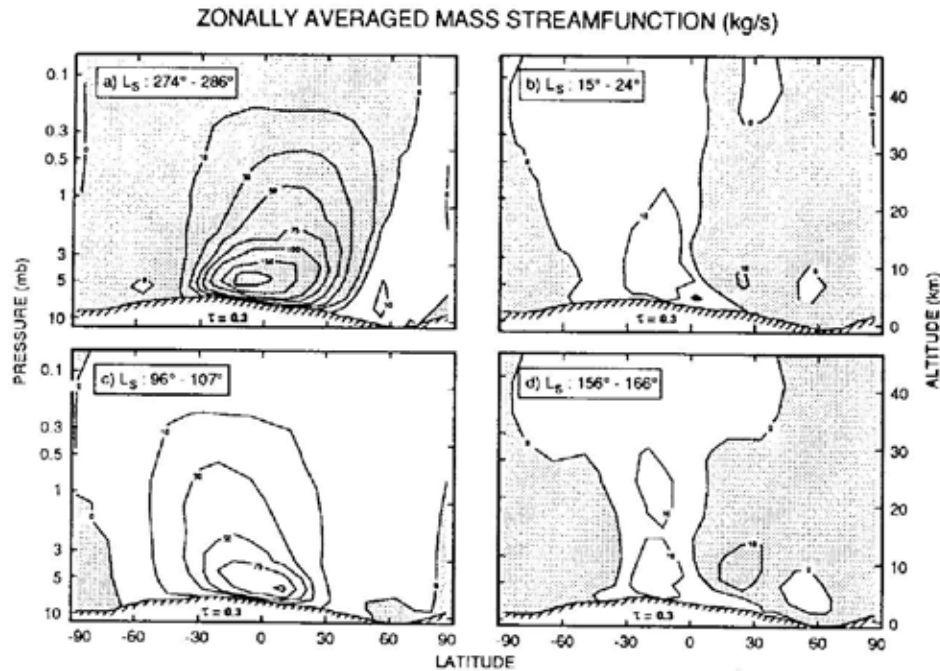
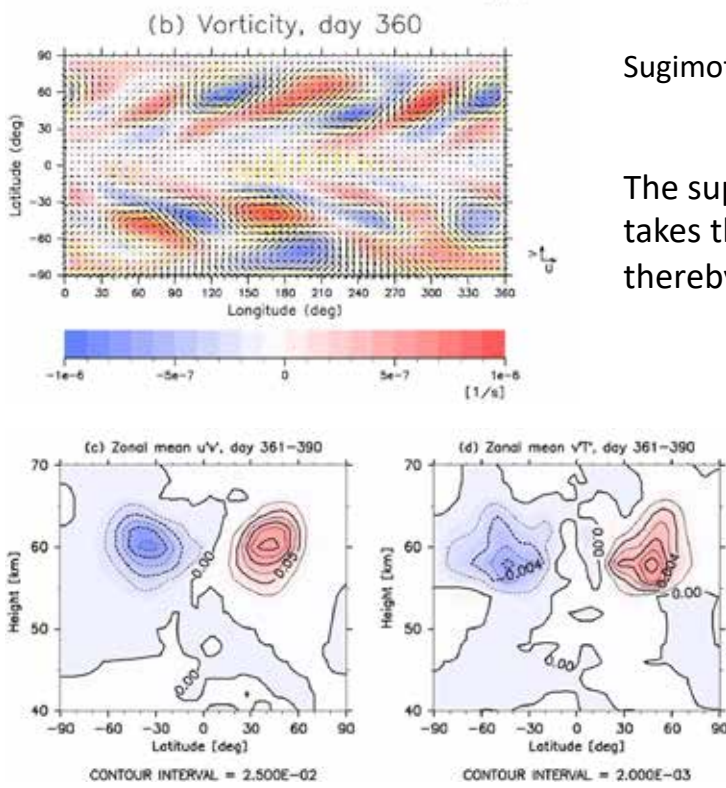


**Fig. 19.** Mass-weighted stream functions computed by the Mars-GCM (Pollack et al. 1990a) for early northern winter (a:  $L_s \approx 280^\circ$ ), early northern spring (b:  $L_s \approx 20^\circ$ ), early northern summer (c:  $L_s \approx 103^\circ$ ) and late northern summer (d:  $L_s \approx 161^\circ$ ). A background dust opacity of  $\tau = 0.3$  was assumed. Flow in the meridional plane is clockwise around minima (negative values are shaded) and anti-clockwise around maxima; winds are strongest where contours are closest.

(Pollack et al 1990)

# Baroclinic instability in Venusian atmosphere



## Driving forces of the zonally-averaged structure

Transformed Eulerian-mean equations:

$$\frac{\partial \bar{u}}{\partial t} + \bar{v}^* \left( \frac{\partial \bar{u}}{\partial y} - f \right) + \bar{w}^* \frac{\partial \bar{u}}{\partial z} = \boxed{\frac{1}{\rho_0} \left( \frac{\partial F^{(y)}}{\partial y} + \frac{\partial F^{(z)}}{\partial z} \right)} \text{ wave forcing}$$

residual mean meridional circulation

$$\bar{v}^* = \bar{v} - \frac{1}{\rho_0} \frac{\partial}{\partial z} \left( \rho_0 \frac{\overline{v' \theta'}}{\bar{\theta}_z} \right)$$

$$\bar{w}^* = \bar{w} + \frac{1}{\rho_0} \frac{\partial}{\partial y} \left( \frac{\overline{v' \theta'}}{\bar{\theta}_z} \right)$$

Eliassen-Palm flux (EP flux)

$$F^{(y)} = -\rho_0 \overline{u' v'}$$

$$F^{(z)} = -\rho_0 \left( \overline{u' w'} - f \frac{\overline{v' \theta'}}{\bar{\theta}_z} \right)$$

$$\frac{\partial \bar{\theta}}{\partial t} + \bar{v}^* \frac{\partial \bar{\theta}}{\partial y} + \bar{w}^* \frac{\partial \bar{\theta}}{\partial z} = \boxed{\bar{Q}} \text{ diabatic heating}$$

木田秀次(1983)

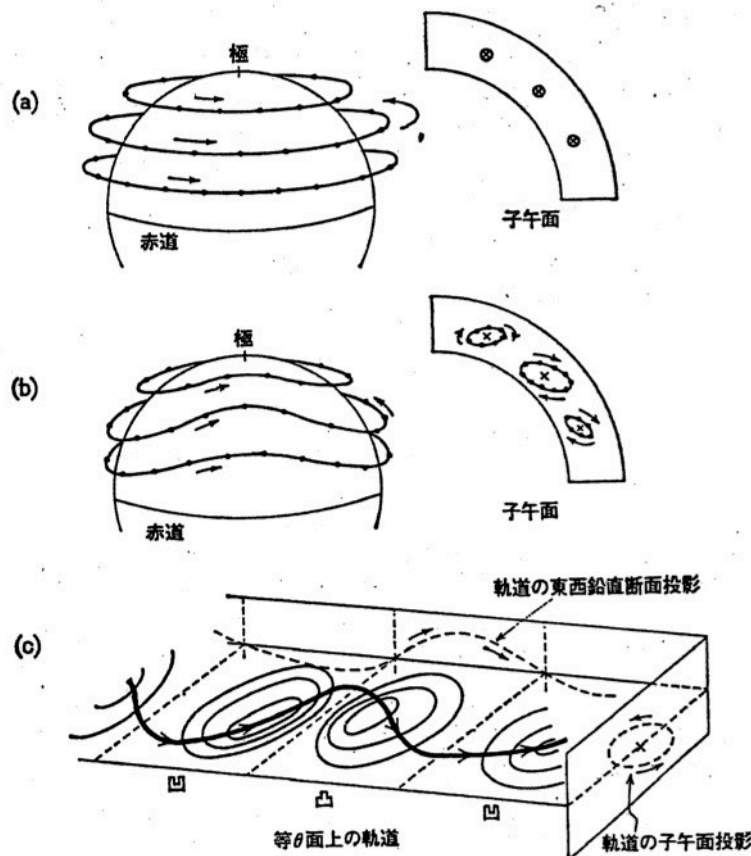


図 5.6 偏西風の中を  
プラネタリー波が鉛直  
伝播するときの空気塊  
の振動。小さい黒点は、  
微小空気塊を表わす。  
(a) 波が不在の場合。  
(b) 波がある場合。×  
印は子午面断面上の元  
の位置。(c) 等温位面上  
の空気塊の軌道。子  
午面投影では主軸が傾  
斜した橢円軌道になる。

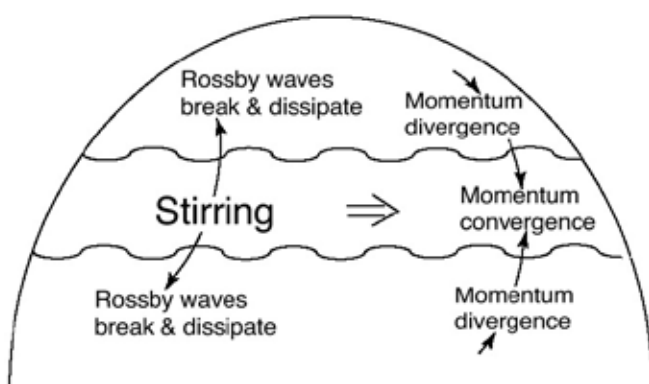
## wave momentum transport

baroclinic instability

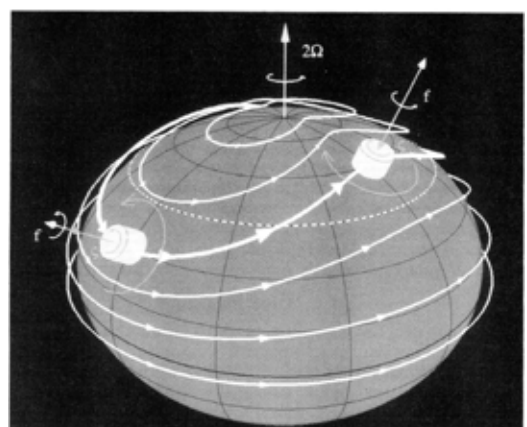
→ generation of Rossby waves

→ Rossby waves take away retrograde (westward) angular momentum from the mid-latitude

→ maintenance of (eastward) mid-latitude jets



(Vallis, 2005)



(Salby, 1996)

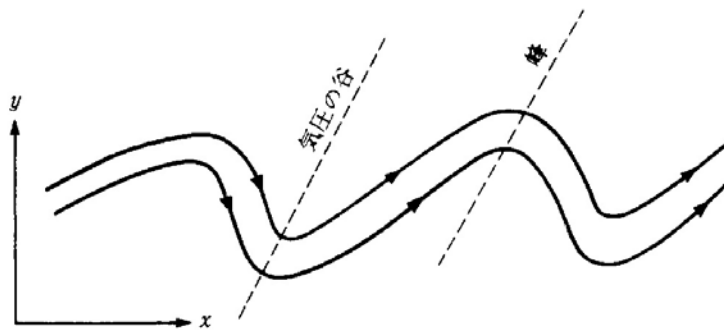


図 8.7 絶対角運動量が偏西風帯の波状擾乱によって極向きに輸送されていることを示す模式図。

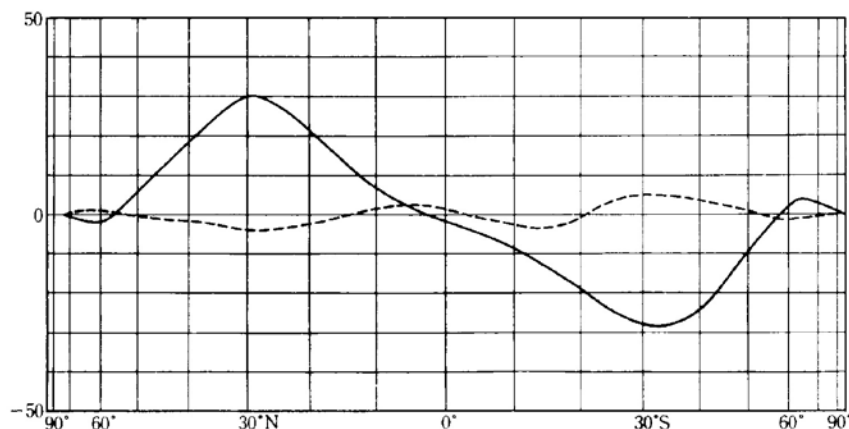
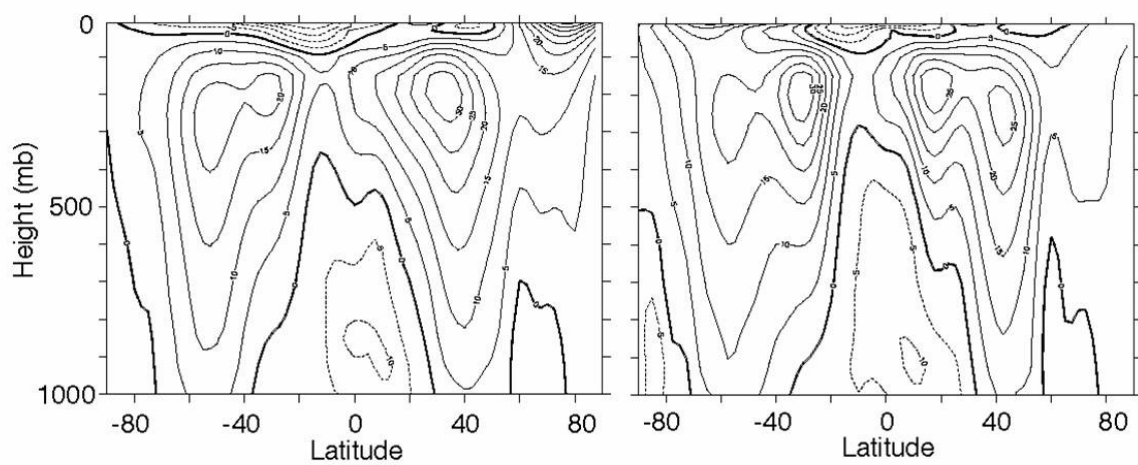


図 8.6 子午面内循環による絶対角運動量の極向き輸送量(破線)と擾乱による輸送量(実線)の年平均(Lorenz, 1967).  
単位は  $10^{18} \text{ kg m}^2 \text{ s}^{-2}$ .

小倉(1978)

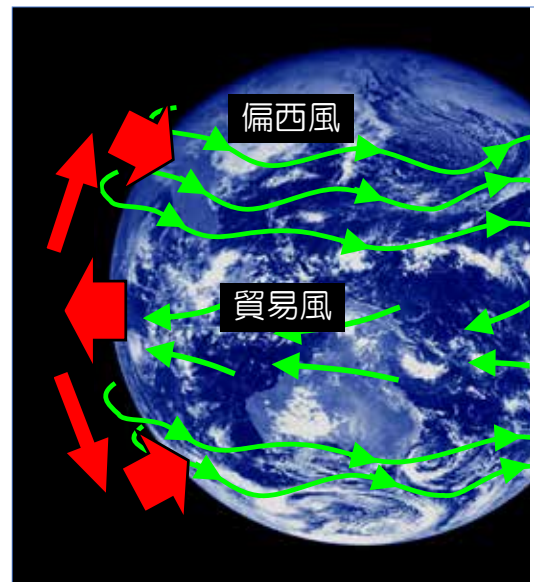


**Fig. 3.1** The time-averaged zonal wind at 150°W (in the mid Pacific) in December-January February (DJF, left), March-April-May (MAM, right). The contour interval is  $5 \text{ m s}^{-1}$ . Note the double jet in each hemisphere, one in the subtropics and one in midlatitudes. The subtropical jets are associated with strong meridional temperature gradient, whereas the midlatitude jets have a stronger barotropic component and are associated with westerly winds at the surface.

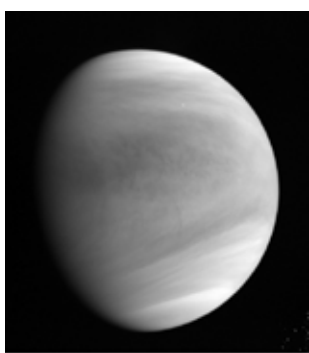
Vallis (2006)

# Angular momentum budget

- 中高緯度：偏西風のため大気が地面を引きずり、大気から固体惑星へ角運動量輸送
- 低緯度：偏東風のため地面が大気を引きずり、固体惑星から大気へ角運動量輸送
- 対流圏：Rossby波の伝播により低緯度から高緯度へ角運動量輸送



## Latitudinal structures



Rotation period 243 days

1 day

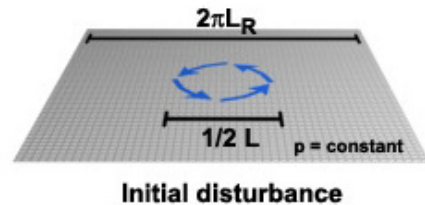
10 hours

# Rossby radius of deformation

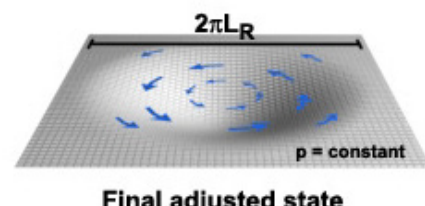
$$L_R = \frac{\sqrt{gH}}{f}$$

$g$  : gravitational acceleration  
 $H$  : depth of the system  
 $f = 2\Omega \cos \theta$  : Coriolis parameter

The characteristic scale at which the velocity field and the pressure field adjust with each other to maintain geostrophic flow



Faster planetary rotation leads to large  $f$ , and then shorter  $L_R$



Parameter study of the atmospheric circulation of Earth-like planets with general circulation models (GCMs)

Williams (1988)

Zonal velocity

white : eastward  
 shade : westward

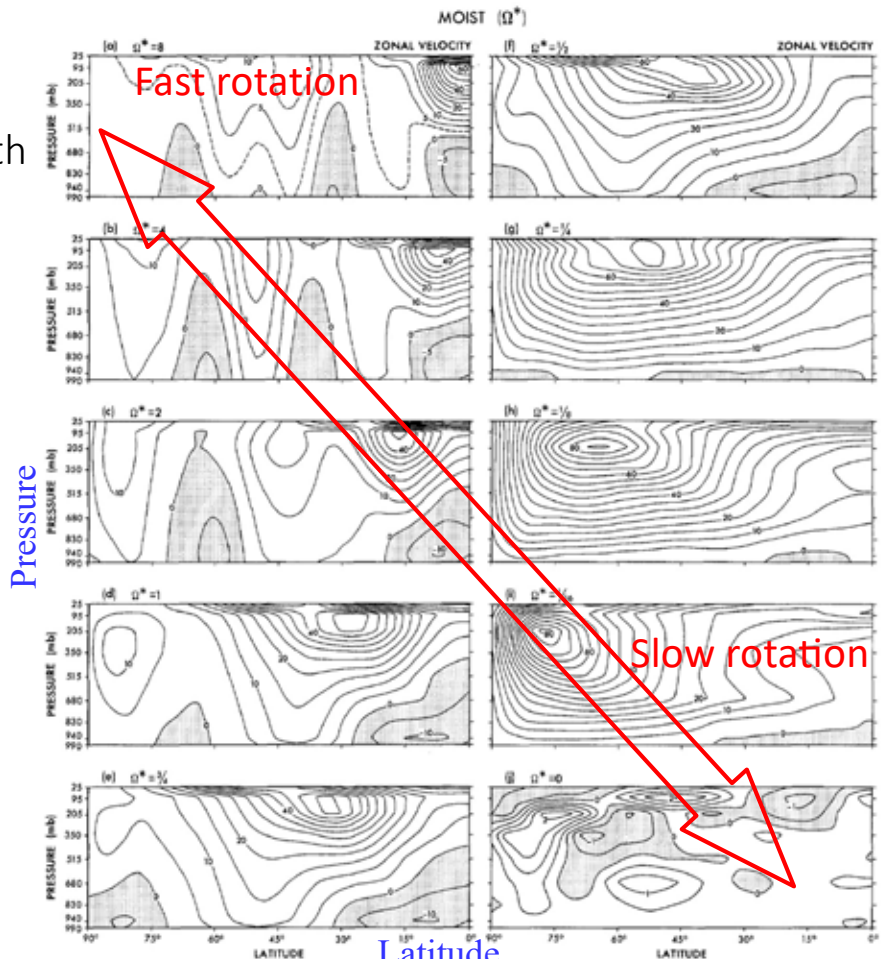


Fig. 2. Meridional distribution of the mean zonal wind for the MOIST model with  $\Omega^* = 0.8$ . Units:  $m s^{-1}$

## Meridional stream function

white : anti-clockwise

shade : clockwise

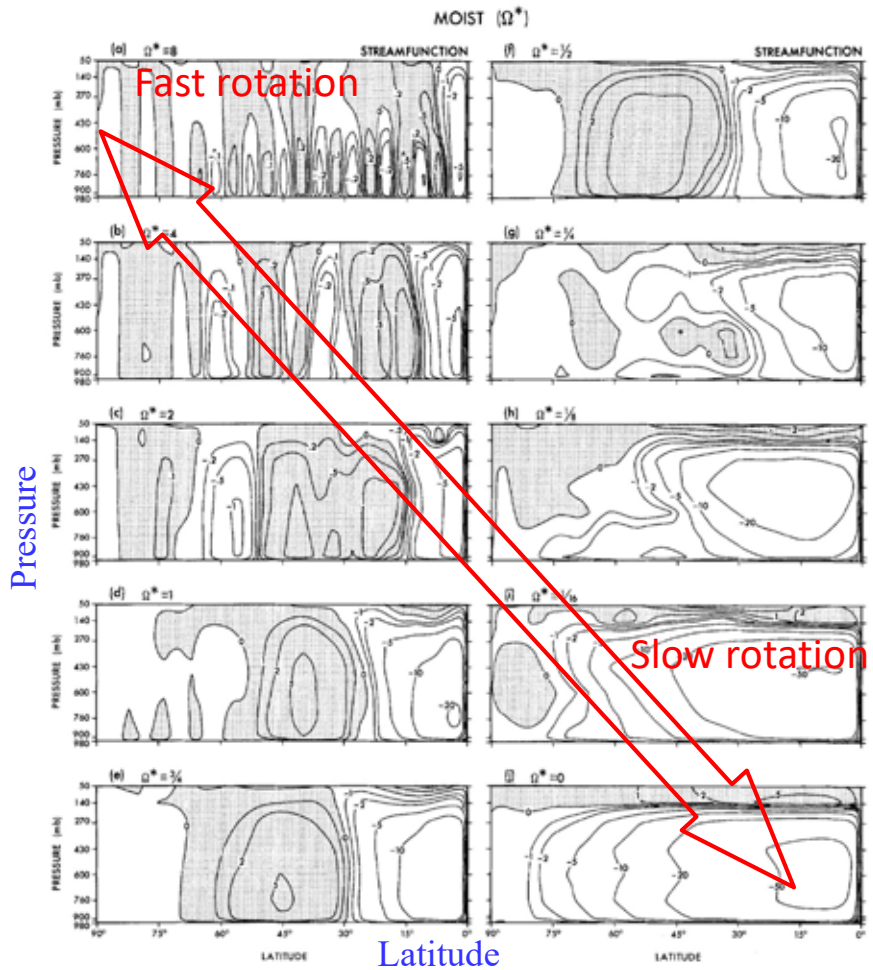


Fig. 3. Meridional distribution of the mean stream function for the MOIST model with  $\Omega^*=0.8$ . Units:  $10^{13} \text{ g s}^{-1}$

## Temperature

white :  $> 220\text{K}$

shade :  $< 220\text{ K}$

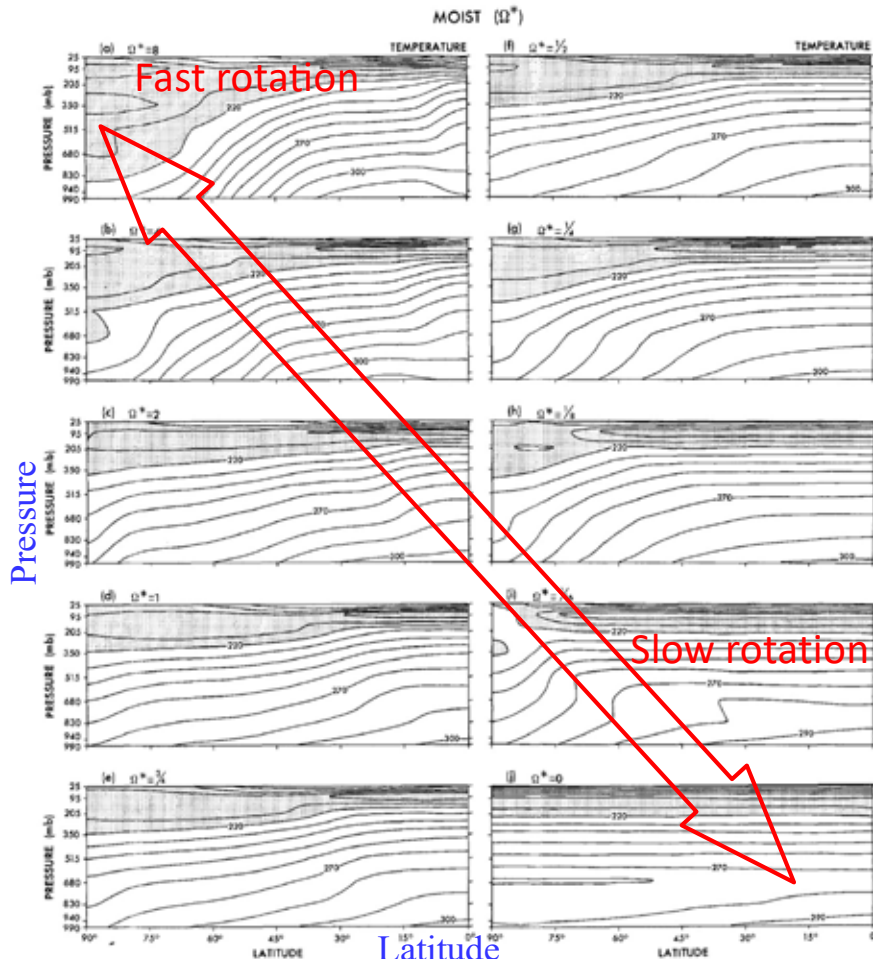


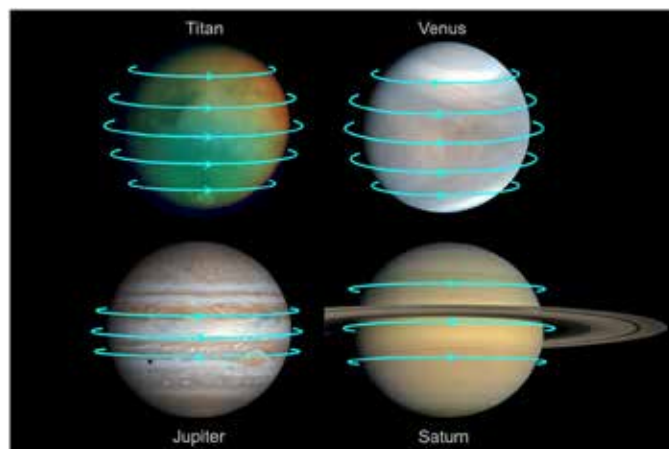
Fig. 4. Meridional distribution of the mean temperature for the MOIST model with  $\Omega^*=0.8$ . Units: K

# Superrotation



taken by Akatsuki UV Imager

## Observed superrotating atmospheres

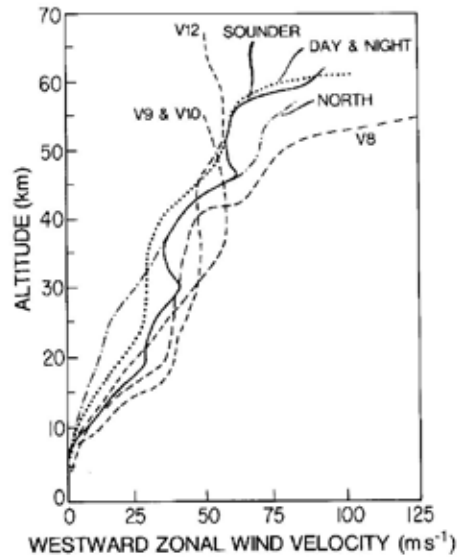


Planet	Radius (km)	Rotation period (days)	Equatorial rotation speed (m/s)	Equatorial wind speed (m/s)	Superrotation index, $s$ , on the equator
Venus	6,052	243	1.81	100–120	55–66
Titan	2,576	16.0	11.7	100–180	8.5–15
Jupiter	69,911	0.41	12,300	60–140	0.005–0.011
Saturn	58,232	0.44	9,540	350–430	0.037–0.045
HD 189733b	79,500	2.2	2600	2400	0.92

# Superrotation of Venus' atmosphere



Zonal winds measured by entry probes



60 times faster rotation of the atmosphere (period=4 Earth days) than the solid planet (period=243 Earth days)

# Superrotation of Venus' atmosphere

Latitudinal profiles of the zonal wind speed at different levels (20–60 km) measured by entry probes

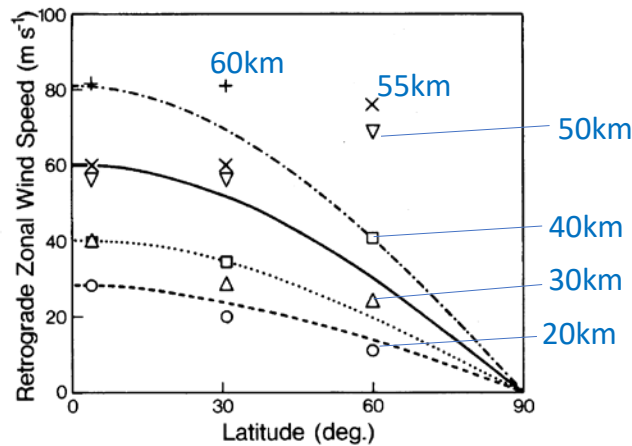
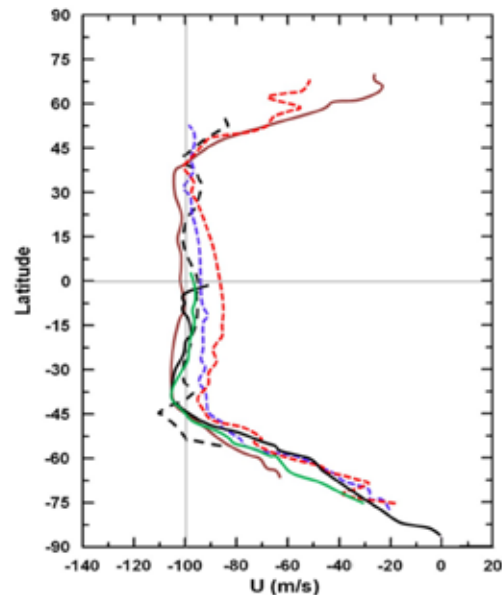


Fig. 10. Latitudinal variation of retrograde zonal wind speeds measured by interferometric tracking of Pioneer Venus probes. The symbols refer to different altitudes: 20 km, (○); 30 km, (Δ); 40 km, (□); 50 km, (▽); 55 km, (×); and 60 km, (+). The curves represent solid body rotation at different rates. It is assumed that the zonal circulation is approximately symmetric about the equator, so the wind speeds for the Day and Night probes can be plotted at 31°N.

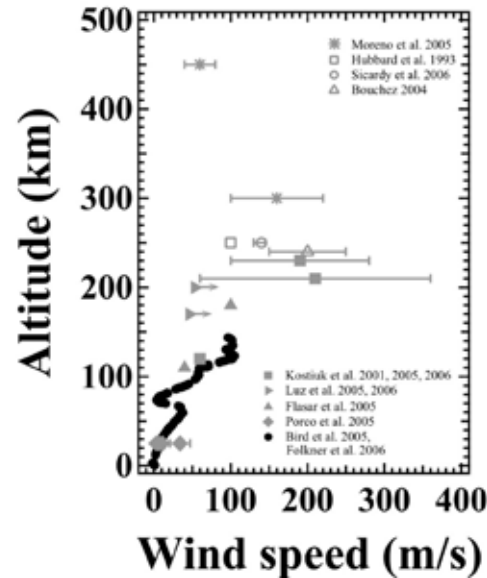
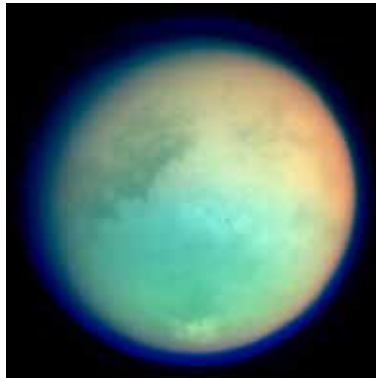
Cloud-tracked winds from various missions



Sánchez-Lavega et al. (2017)

# Superrotation of Titan's atmosphere

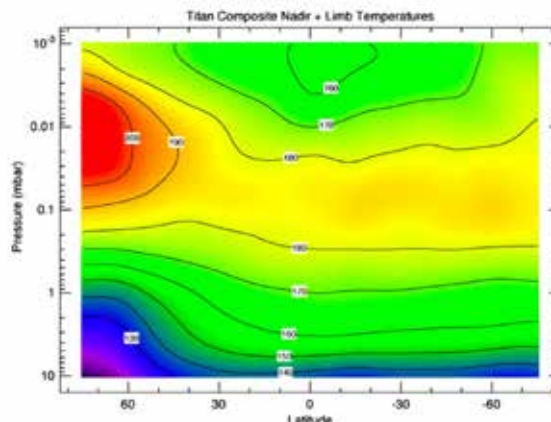
Hörst et al. 2017



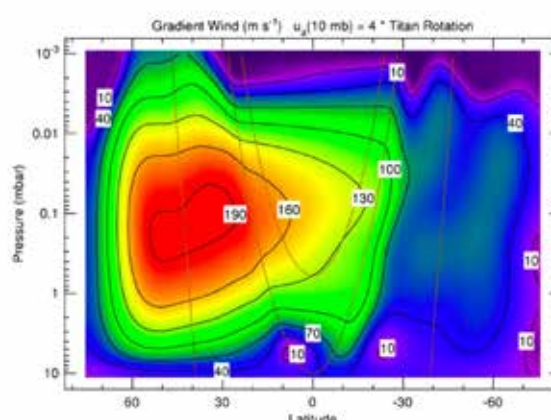
The atmosphere circulates 10 times faster than the rotation of the solid planet.

Infrared observation by CIRS on NASA Cassini (northern winter)

Achterberg et al. 2008



Zonal-mean temperature



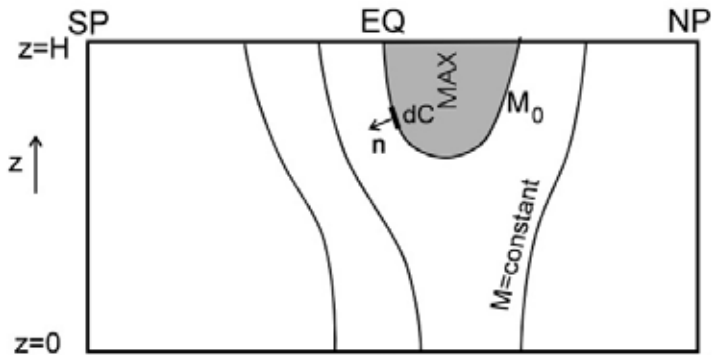
Zonal winds calculated from the temperature using thermal wind relation

Fig. 9. Zonal mean temperatures from all limb and nadir maps. Retrieved temperatures were averaged in  $5^\circ$  latitude bins, then smoothed with a  $10^\circ$  boxcar function applied three times. Contours are labeled in K.

Fig. 10. Zonal winds calculated from the temperatures in Fig. 9 from the gradient wind equation, assuming solid-body rotation at the 10 mbar level at four times Titan's rotation rate. Wind speed contours (black lines) are labeled in  $m s^{-1}$ . The gray lines indicate cylindrical surfaces parallel to the rotation axis along which the gradient wind equation is integrated. Equatorward and above the gray line tangent to the equator at 10 mbar, the winds are unconstrained by the gradient wind equation, and have been linearly interpolated on constant pressure surfaces.

# Hide's theorem

Hide (1969) showed that non-axisymmetric eddies (waves) are needed to maintain the jets aloft the surface and that the required momentum convergence should be provided by upgradient angular momentum transport.



(Vallis, 2005)

## Difference between Venus and Titan

- hot Venus (740K) vs. cold Titan (90K)
- large Venus (radius=6050km) vs. small Titan (2575km)

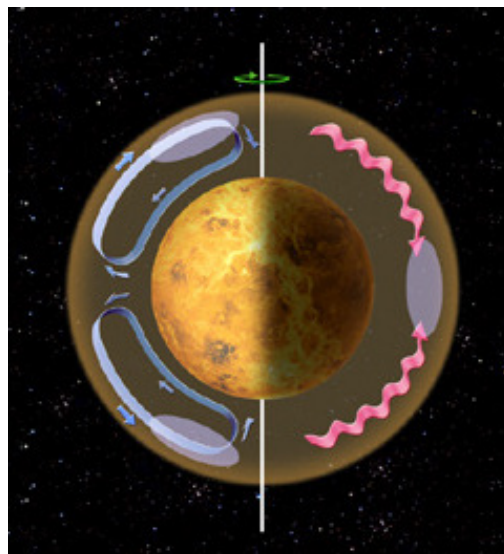
## Similarity between Venus and Titan

- slow rotation (period = 243 days for Venus, 16 days for Titan)
- thick aerosol layer
- long radiative relaxation time (30 years for Venus, 100 years for Titan)

# Hypothesis: Acceleration by meridional circulation and horizontal eddies (Gierasch, 1974; Rossow & Williams, 1979)

## Hadley circulation

transports angular momentum poleward, thereby creating high-latitude jets.



## Horizontal eddies

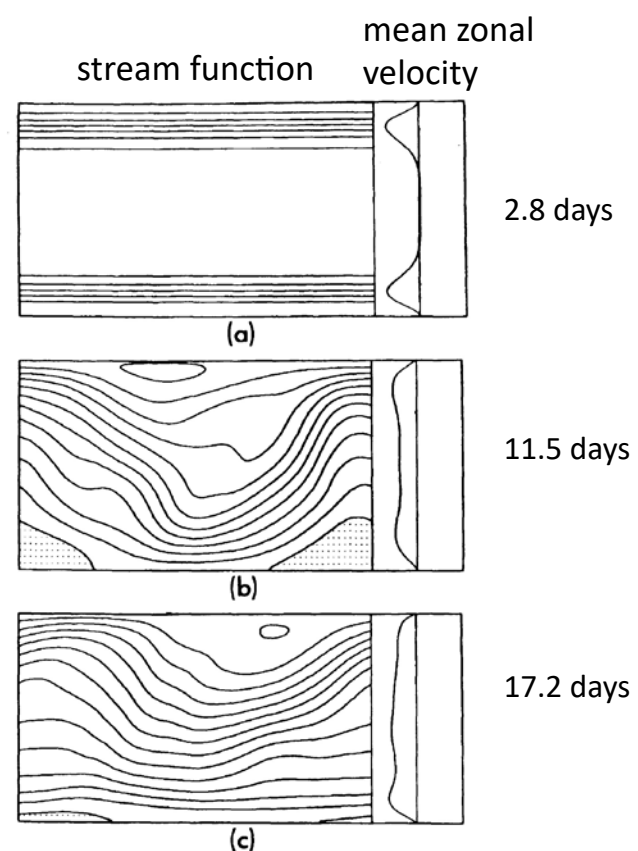
transport angular momentum equatorward to smooth out the differential rotation of the atmosphere.

The combination of the two processes leads to an accumulation of angular momentum in the equatorial upper atmosphere.

## 2D simulation in a slowly-rotating system

(Williams and Rossow 1979)

- planetary rotation same as Venus
- momentum forcing at high latitudes
- baroclinic instability, followed by generation of large-scale waves and equatorward momentum transport



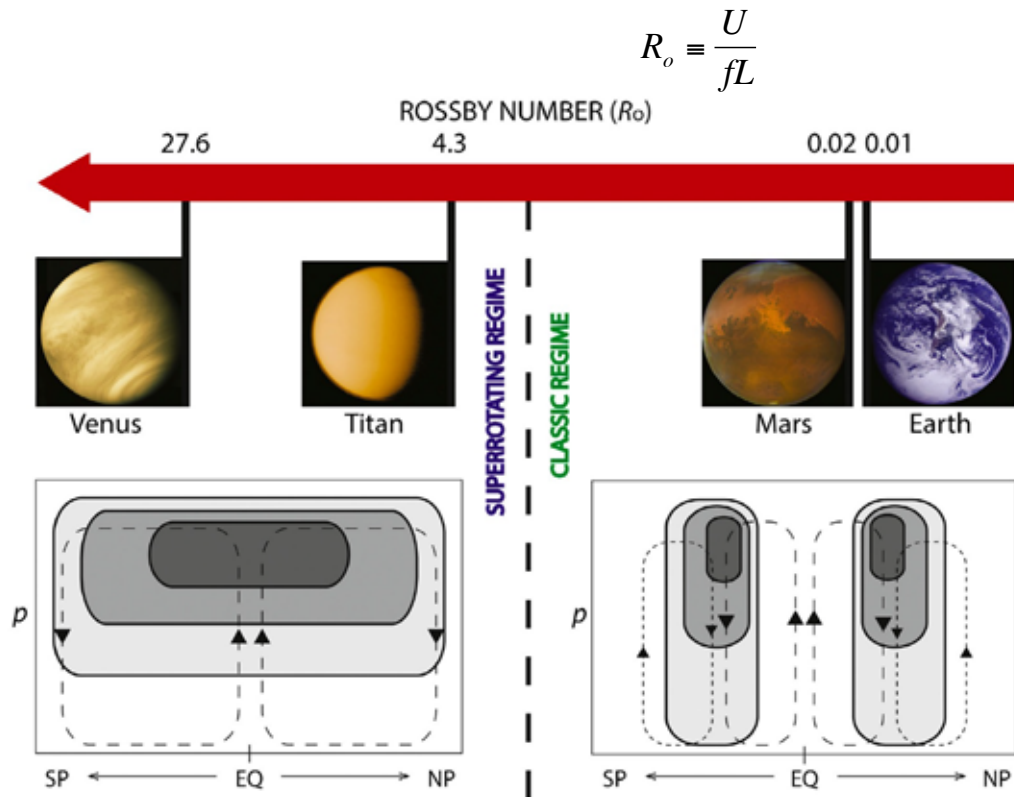
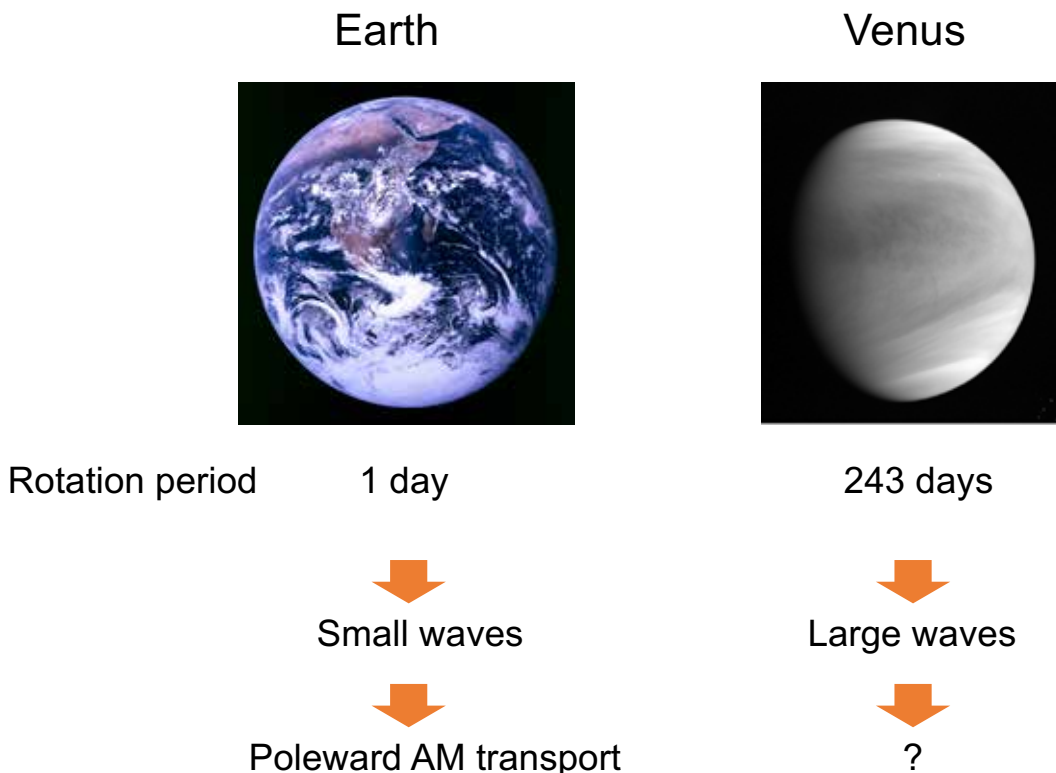


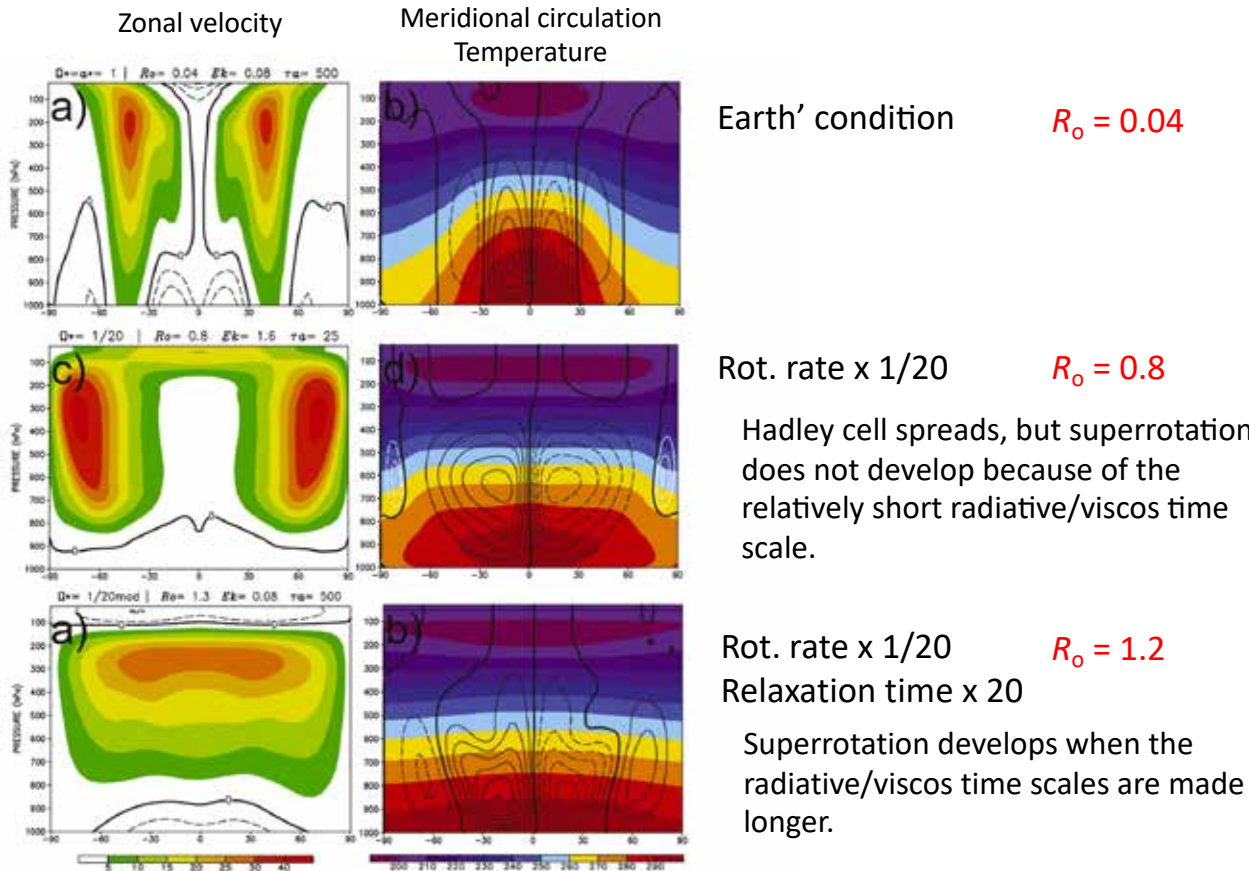
**Fig. 1.** Schematic view of the different Rossby numbers ( $R_o$ ) and circulation regimes found on the terrestrial bodies of the Solar System with substantial atmospheres.  $R_o$  was computed based on typical scales of zonal winds (around  $100 \text{ m s}^{-1}$  for Venus and Titan and  $10 \text{ m s}^{-1}$  for Earth and Mars), rotation rate, and planetary radius. The lower panels depicts a hypothetical vertical cross section of zonal mean zonal wind (shaded, arbitrary scale) and mean overturning circulation (dashed lines, arbitrary scales) characteristic of each body's atmospheres. See text for more details (photo credits: NASA/JPL).

Dias Pinto & Mitchell (2014)

## Difference in wave characteristics between Earth and Venus

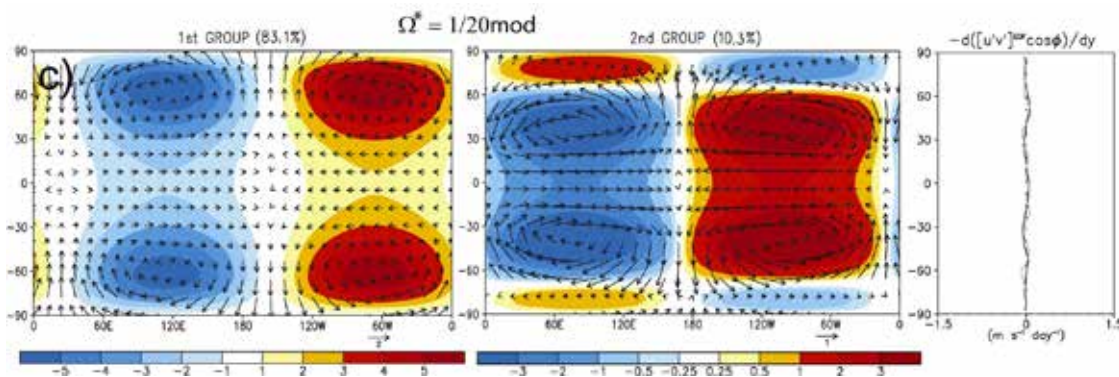


# Parameter dependence in Earth-like GCM (Dias Pinto & Mitchell 2014)



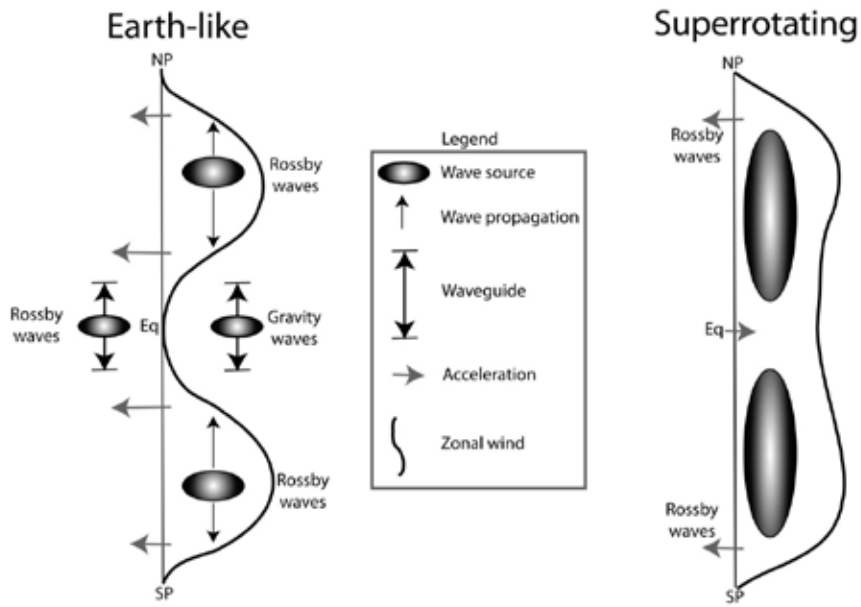
Wave structures (EOF 1, 2)

Rot. rate x 1/20 , Relaxation time x 20



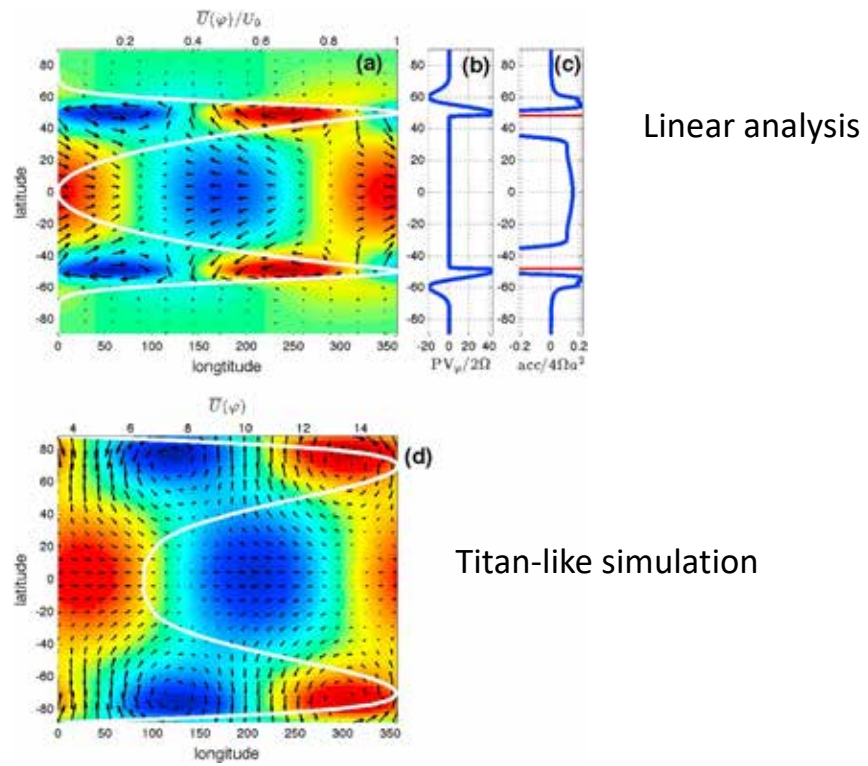
In order for superrotation to develop, the relaxation time needs to be long in addition to a large Rossby number.  
 → Condition on Venus and Titan

# How waves work?



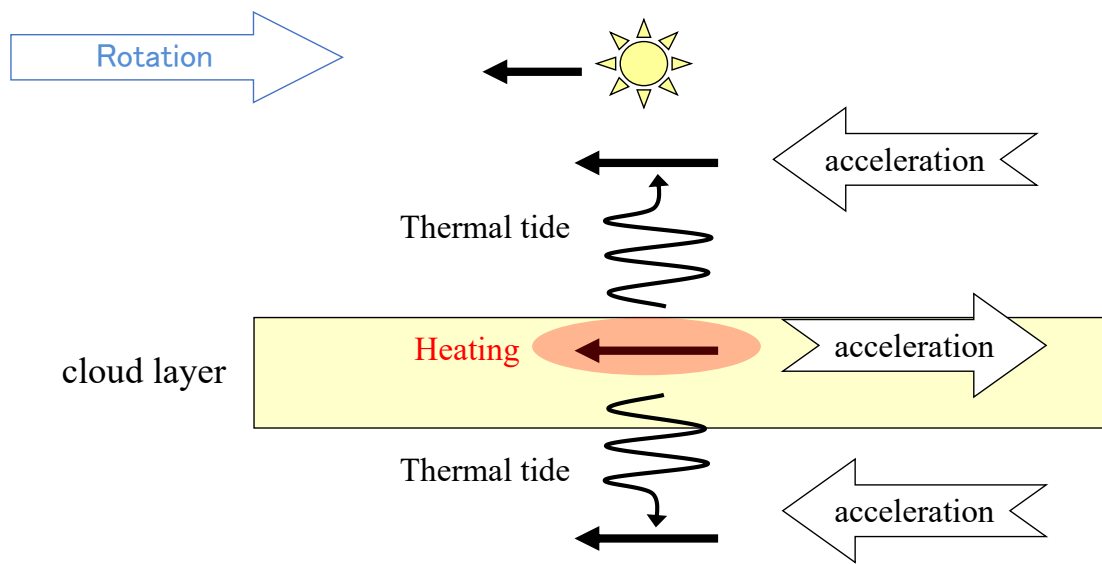
Mitchell & Vallis (2010)

Rossby-Kelvin instability  
(Sakai 1989; Iga and Matsuda 2005; Wang & Mitchell 2014)



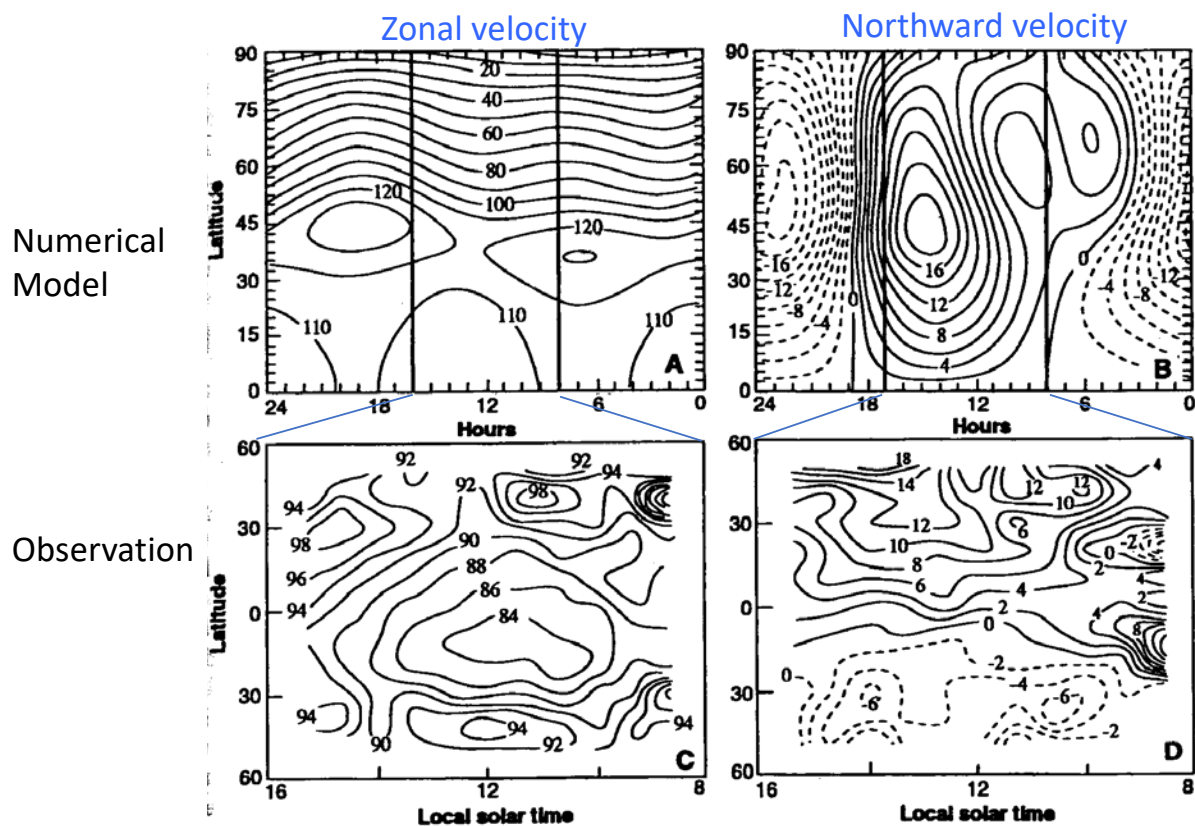
Wang & Mitchell (2014)

## Hypothesis: Acceleration by thermal tides (Fels & Lindzen 1974)



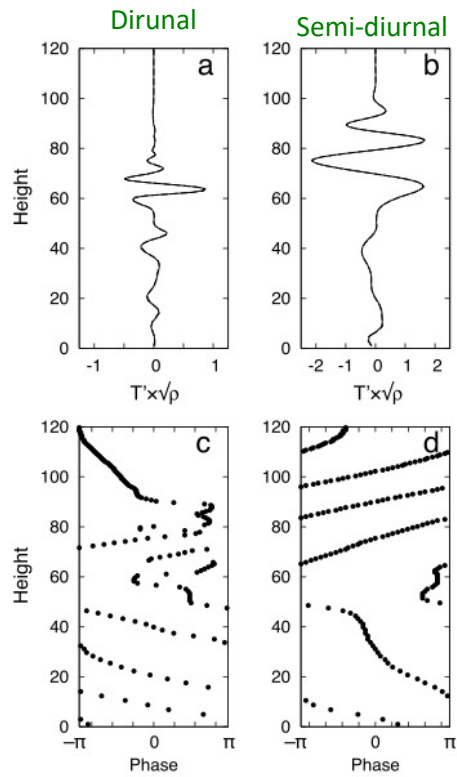
太陽光加熱域の移動により、東向き運動量を持つ重力波が励起されて上下に伝搬 → 雲層が反動で西向きに加速

### Thermal tides at the cloud top

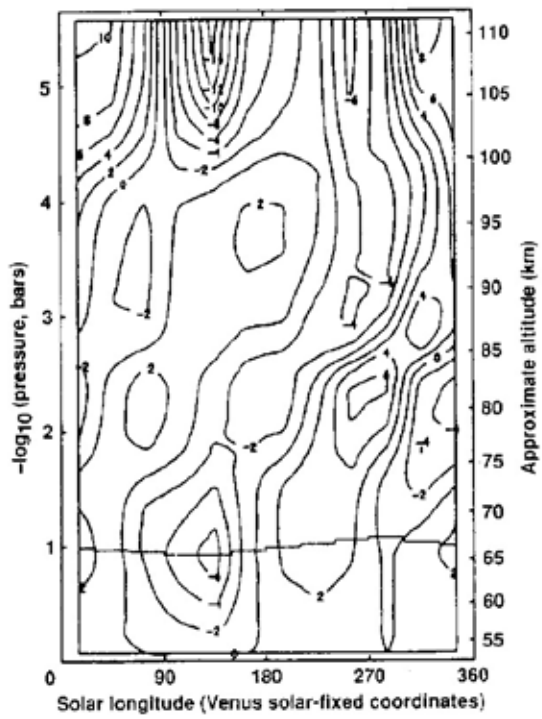


# Vertical structure of thermal tides in Venus's atmosphere

Linear solution (Takagi & Matsuda, 2006)



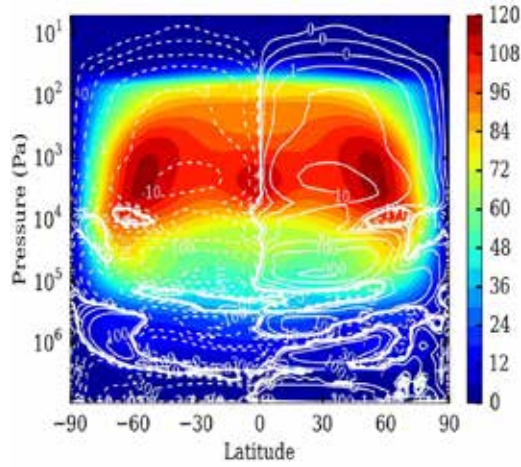
Temperature perturbation  
(Schofield & Taylor 1983)



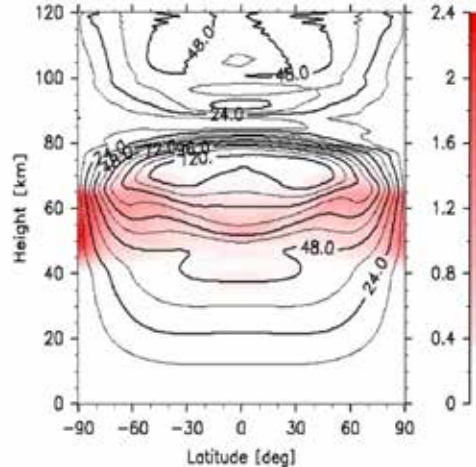
## Numerical models

### Zonal winds

Garate-Lopez and Lebonnois (2018)



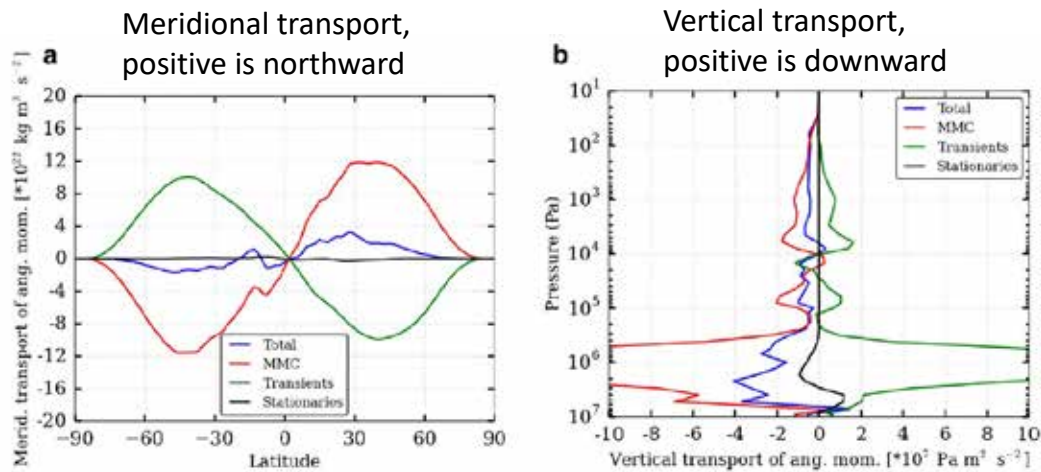
Sugimoto et al. (2014)



# Numerical models

## Transport of angular momentum

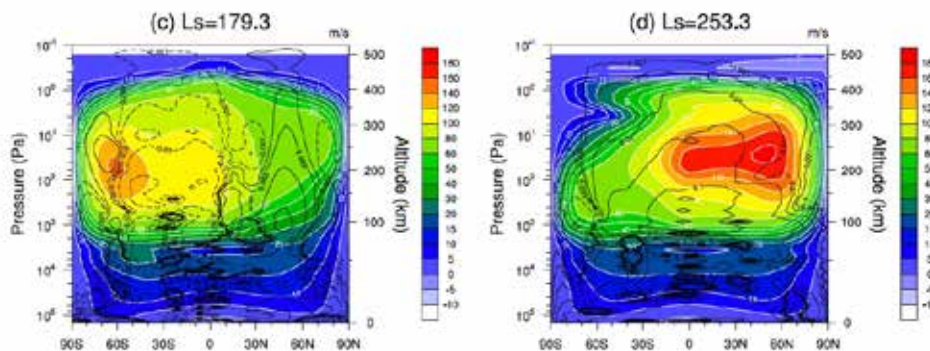
Lebonnois et al. (2016)



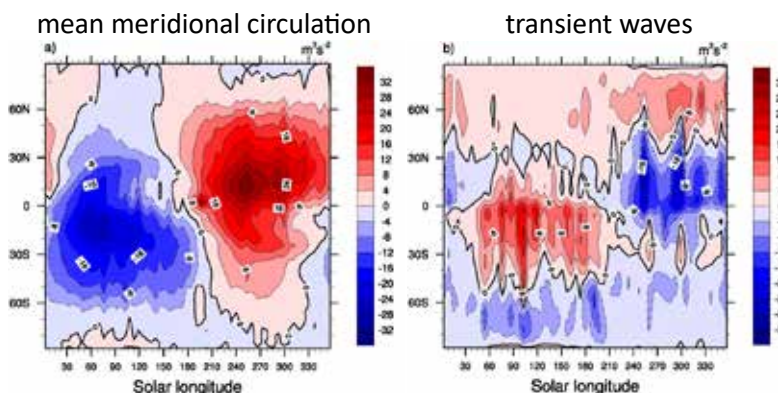
## Numerical model of Titan

Lebonnois et al. (2012)

### Mean zonal wind and meridional stream function

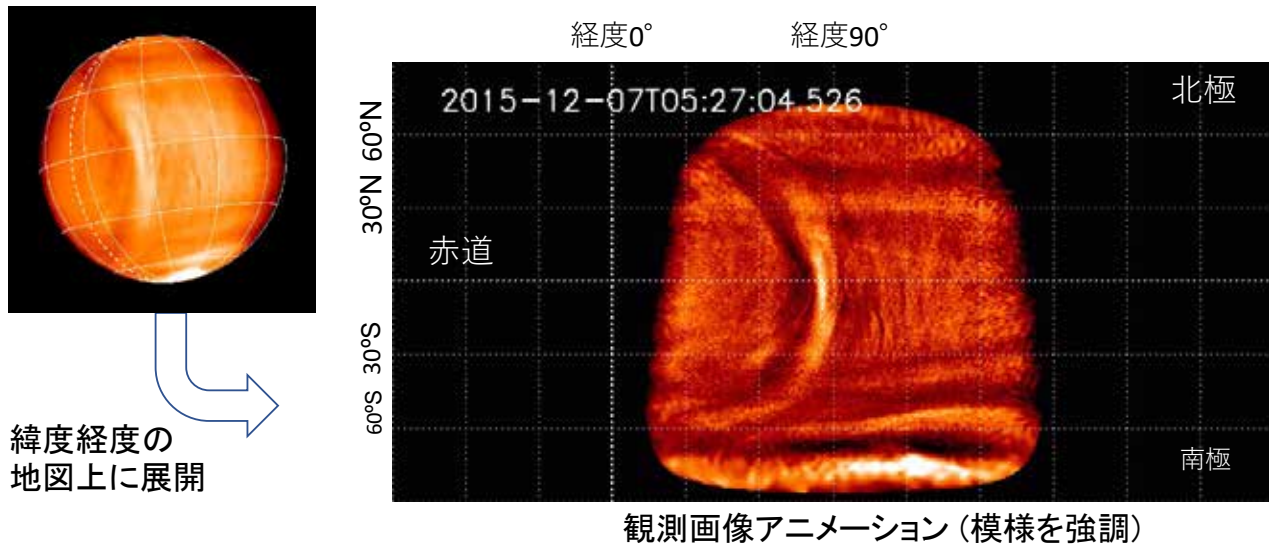


### Seasonal variations of the vertically-integrated latitudinal transport of angular momentum



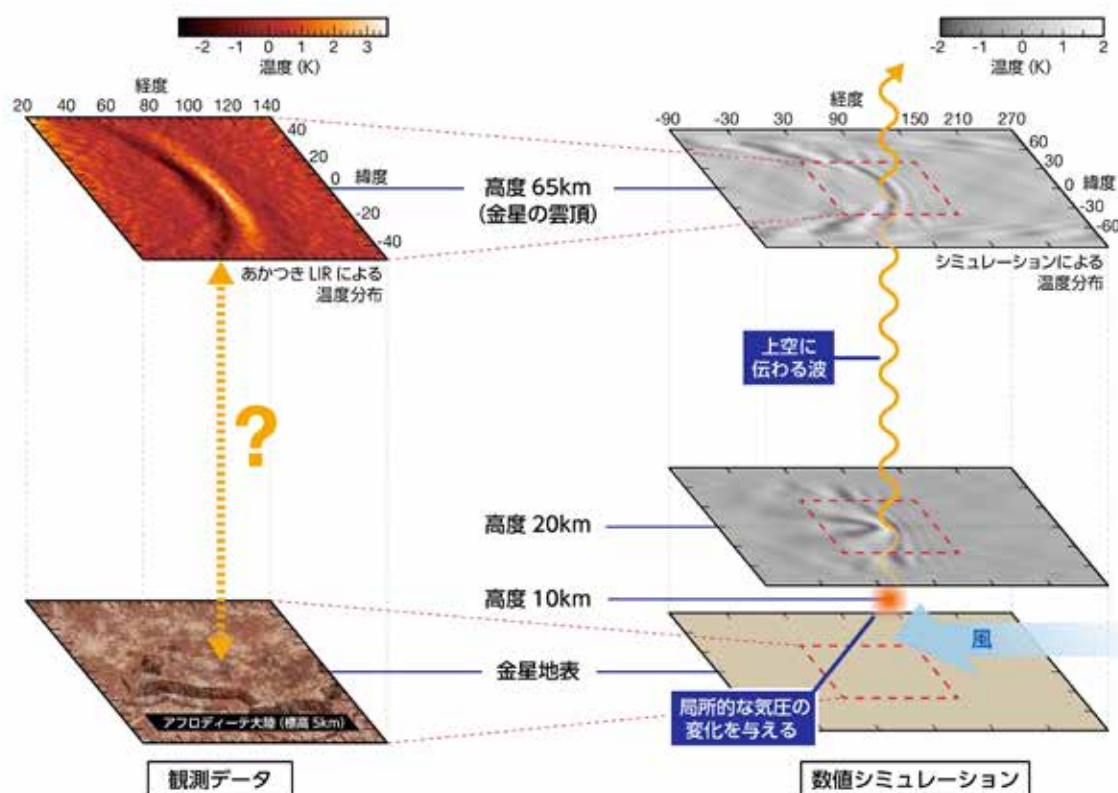
# Bow-shaped stationary features discovered by Akatsuki

Almost stationary in the superrotating background atmosphere

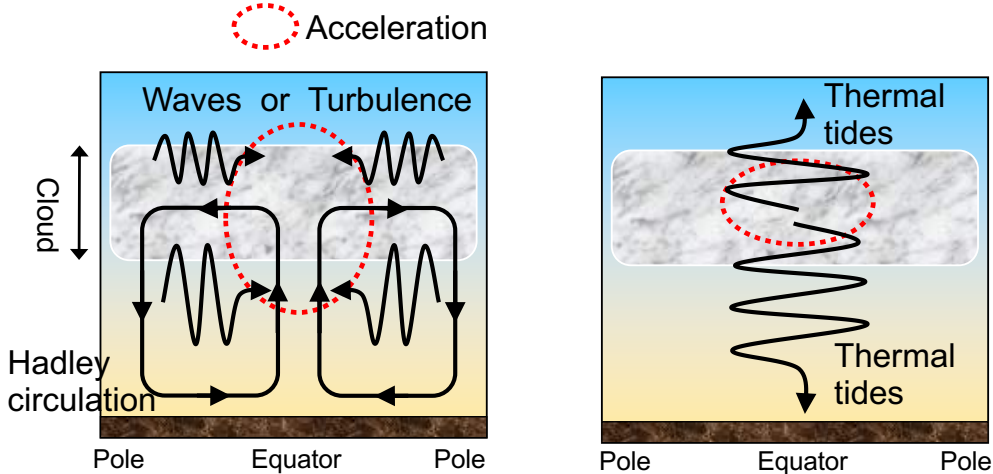


神山(NICT)作成

## Mountain waves ?



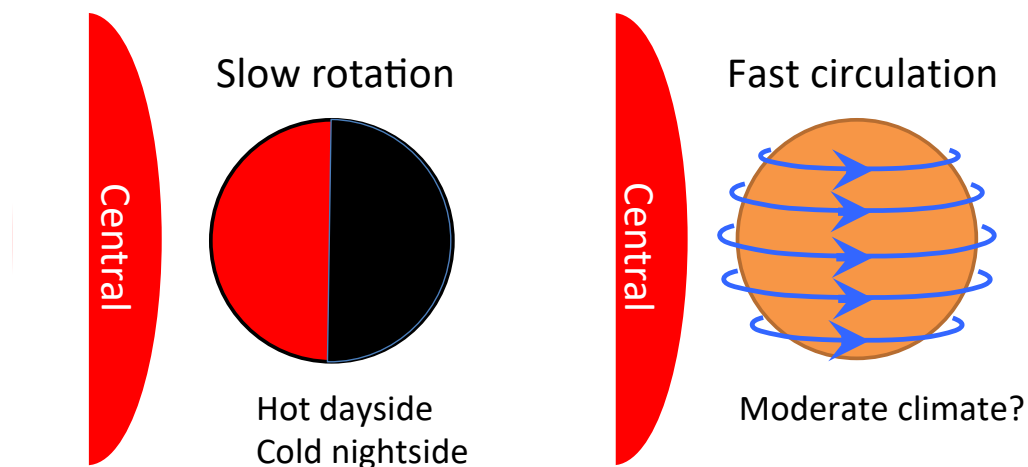
# Candidate mechanisms of super-rotation

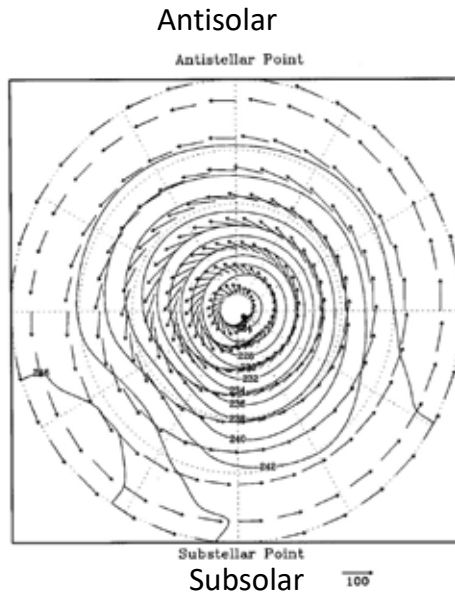


- Both mechanisms predict anti-superrotational winds near the surface.
  - On the other hand, existence of mountain waves requires superrotational winds prevailing from the cloud level to the surface.
- Open question

## Implications for exoplanets

- Tidally-locked planets are mostly slow rotators like Venus.
- Super-rotation can redistributes thermal energy along the local time on such planets.



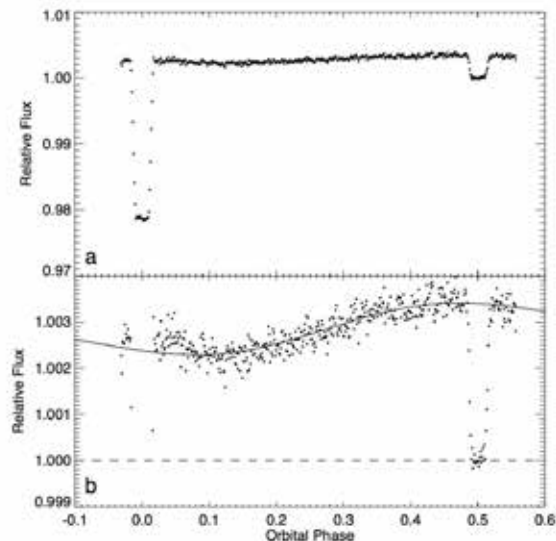


Polar view of the atmospheric circulation and temperature distribution at 20 km altitude on a synchronously rotating terrestrial planet (Joshi et al., 1997)

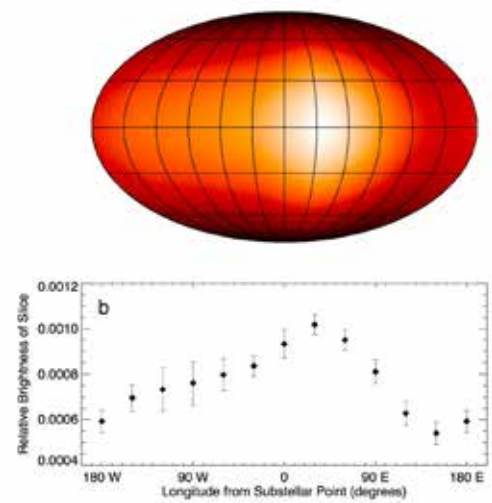
A map of the day-night contrast of the extrasolar planet HD 189733b (Knutson et al. 2007)

A minimum brightness temperature of  $973 \pm 33$  K and a maximum brightness temperature of  $1212 \pm 11$  K at a wavelength of 8 microns, indicating that energy from the irradiated dayside is efficiently redistributed throughout the atmosphere

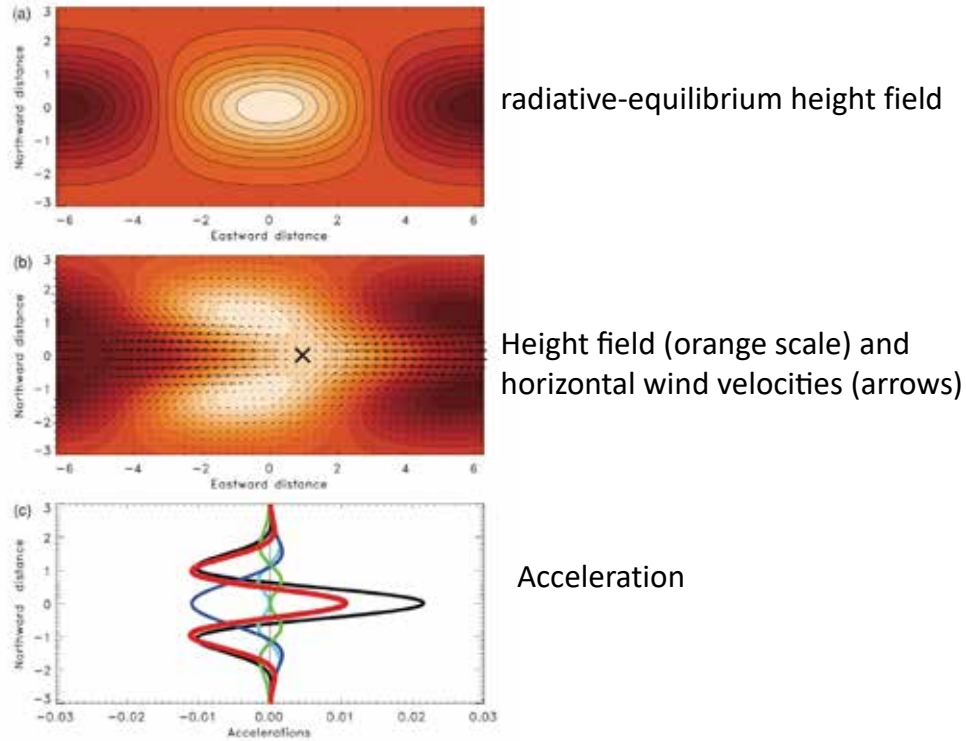
Observed phase variation for HD 189733b, with transit and secondary eclipse visible.



Brightness estimates for 12 longitudinal strips on the surface of the planet

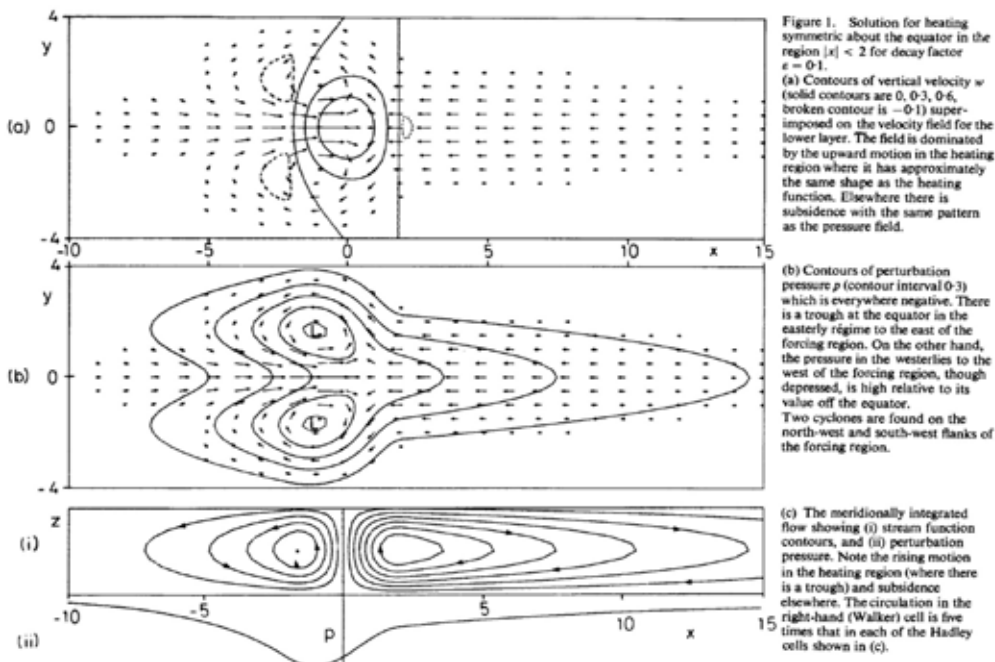


Linear, analytic solution for parameters relevant to hot, tidally locked exoplanets  
(Showman & Polvani 2011)



## Matsuno-Gill pattern (Matsuno 1966; Gill 1980)

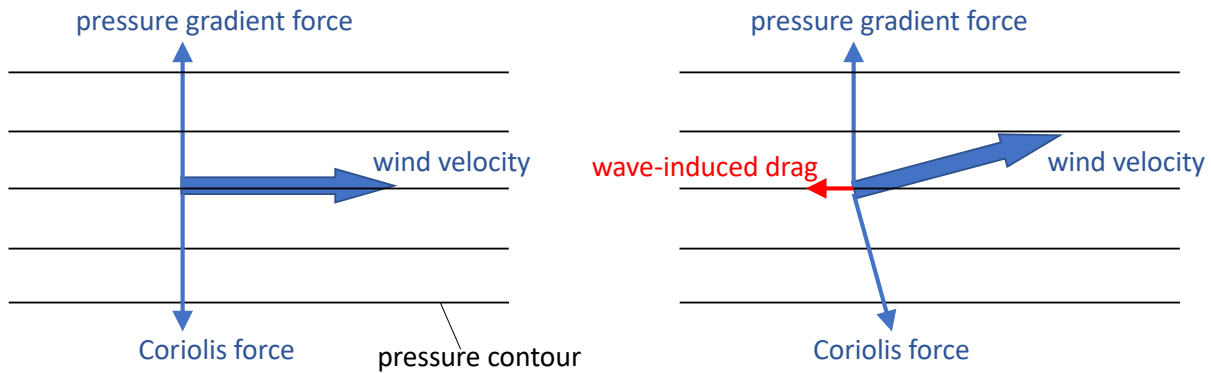
- Heat-induced tropical circulation composed of Rossby wave and Kelvin wave
- Plays crucial roles in Earth's troposphere



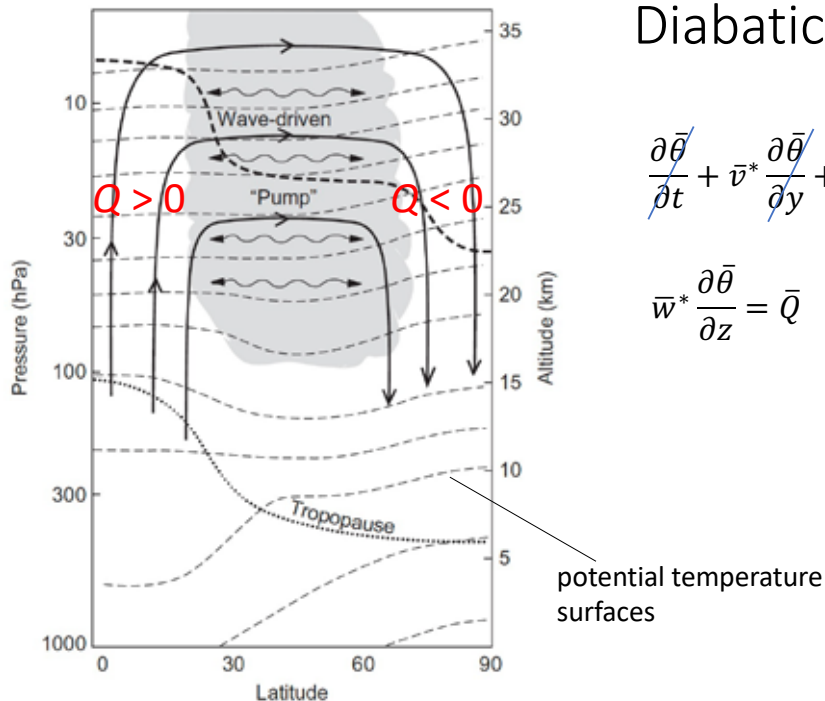
# Wave-driven meridional circulation

$$\frac{\partial \bar{u}}{\partial t} + \bar{v}^* \left( \frac{\partial \bar{u}}{\partial y} - f \right) + \bar{w}^* \frac{\partial \bar{u}}{\partial z} = \boxed{\frac{1}{\rho_0} \left( \frac{\partial F^{(y)}}{\partial y} + \frac{\partial F^{(z)}}{\partial z} \right)} \quad \text{wave forcing}$$

$$f \bar{v}^* = \frac{1}{\rho_0} \left( \frac{\partial F^{(y)}}{\partial y} + \frac{\partial F^{(z)}}{\partial z} \right)$$



Earth's stratospheric meridional circulation (Holton 2012)



Diabatic circulation

$$\frac{\partial \bar{\theta}}{\partial t} + \bar{v}^* \frac{\partial \bar{\theta}}{\partial y} + \bar{w}^* \frac{\partial \bar{\theta}}{\partial z} = \bar{Q} \quad \text{diabatic heating}$$

$$\bar{w}^* \frac{\partial \bar{\theta}}{\partial z} = \bar{Q}$$

potential temperature surfaces

# Earth's mean meridional circulation in the troposphere

Holton 2004

Eulerian-mean  
 $(\bar{v}, \bar{w})$

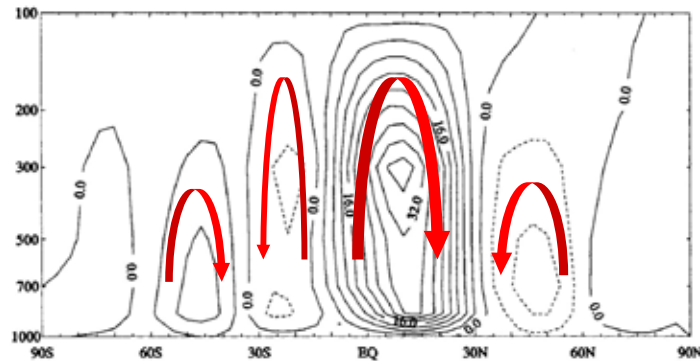
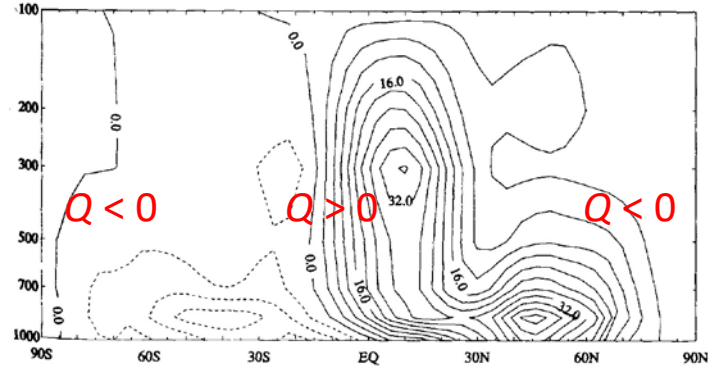
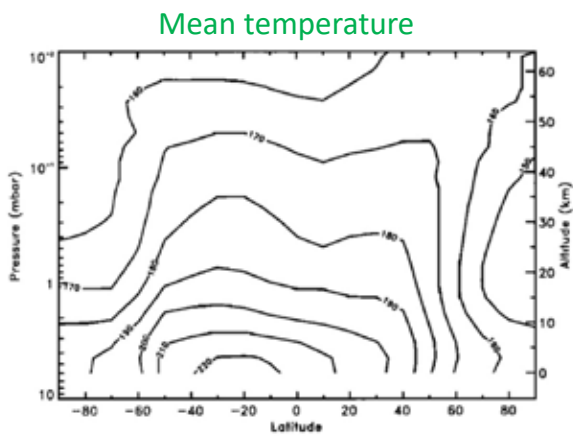


Fig. 10.7 Streamfunction (units:  $10^2 \text{ kg m}^{-1} \text{s}^{-1}$ ) for the observed Eulerian mean meridional circulation for Northern Hemisphere winter, based on the data of Schubert et al. (1990).

Lagrangian-mean  
 $(\bar{v}^*, \bar{w}^*)$



## Meridional circulation of Mars atmosphere (Santee & Crisp 1995)



**Figure 1a.** Diurnal-mean temperatures obtained by averaging the 1400 LT and 0200 LT temperature maps retrieved from the Mariner 9 IRIS spectra in Paper I. For consistency with the results of Paper I, the vertical coordinate in this and all subsequent figures is the atmospheric pressure  $p$ . The approximate altitude  $z$  corresponding to a given pressure level is also included in these figures (see section 2.1). This correlation of altitude with pressure is based on the following values:  $p_s = 6.0 \text{ mbar}$ ,  $R = 191.0 \text{ J K}^{-1} \text{ kg}^{-1}$ ,  $g = 3.74 \text{ m/s}^2$ , and  $T_0 = 196 \text{ K}$  (the globally and diurnally averaged value of the atmospheric temperature at the surface), resulting in a mean scale height  $H = 10 \text{ km}$ .

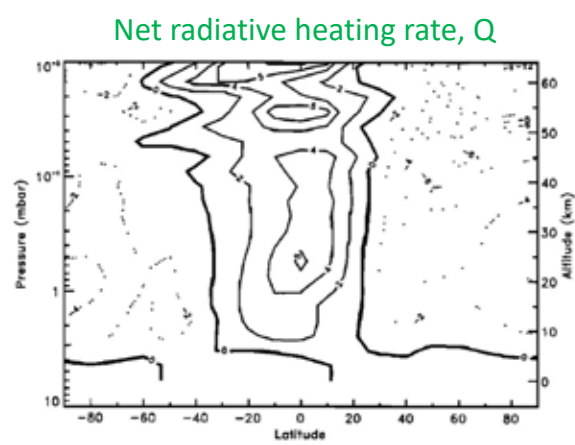


**Figure 3.** Net radiative heating rates ( $\text{K}/\text{d}$ ) calculated from retrieved IRIS temperatures and dust abundances using the radiative transfer model described by Crisp [1990] and in the appendix of Santee [1993]. Negative contours are dashed, the zero contour is thicker, and the contour interval is nonuniform.

# Meridional circulation of Mars atmosphere (Santee & Crisp 1995)

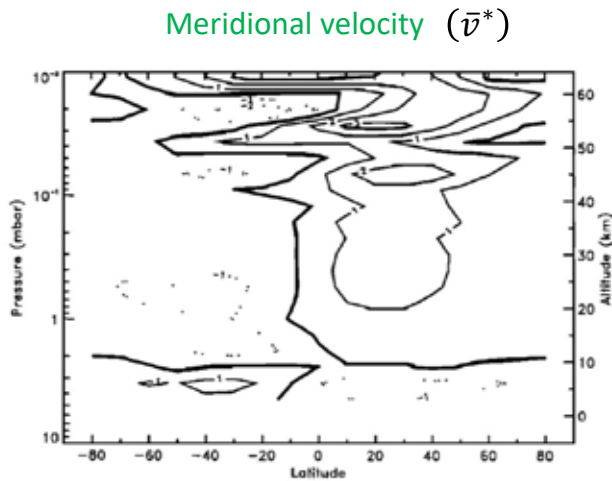


**Figure 4a.** Diabatic meridional velocity, in m/s. Positive values represent northward winds, negative contours are dashed, and the zero contour is thicker.

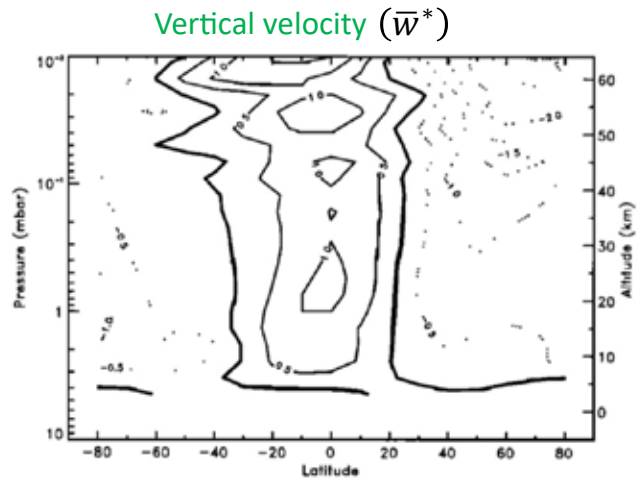


**Figure 4b.** Diabatic vertical velocity, in cm/s. Positive values represent upward winds, negative contours are dashed, and the zero contour is thicker.

# Meridional circulation of Mars atmosphere (Santee & Crisp 1995)

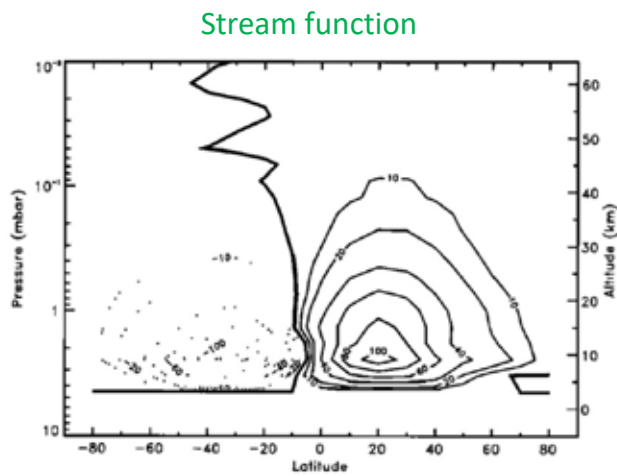


**Figure 4c.** Mass-weighted stream function,  $\Psi_m$ , in units of  $10^7$  kg/s. Positive values represent clockwise flow, negative contours are dashed, the zero contour is thicker, and the contour interval is nonuniform.

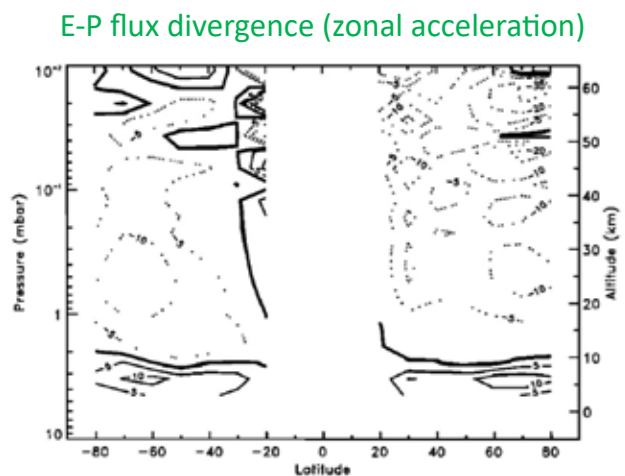


**Figure 5.** Eliassen-Palm flux divergence  $((\rho a \cos \phi)^{-1} \nabla \cdot \mathcal{F})$  in units of  $ms^{-1}/d$ . Negative contours are dashed, the zero contour is thicker, and the contour interval is nonuniform.

# Meridional circulation of Venus atmosphere

Lee et al. (2015)

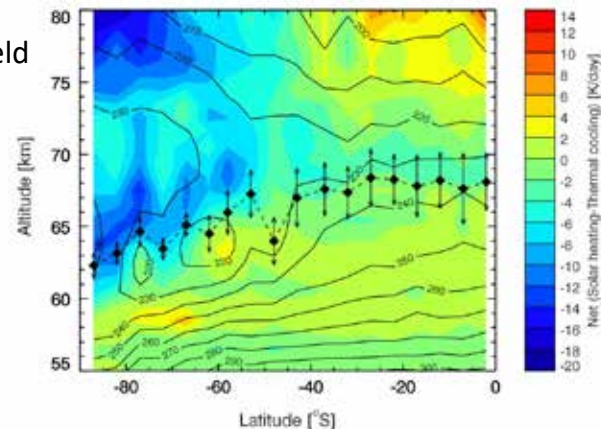
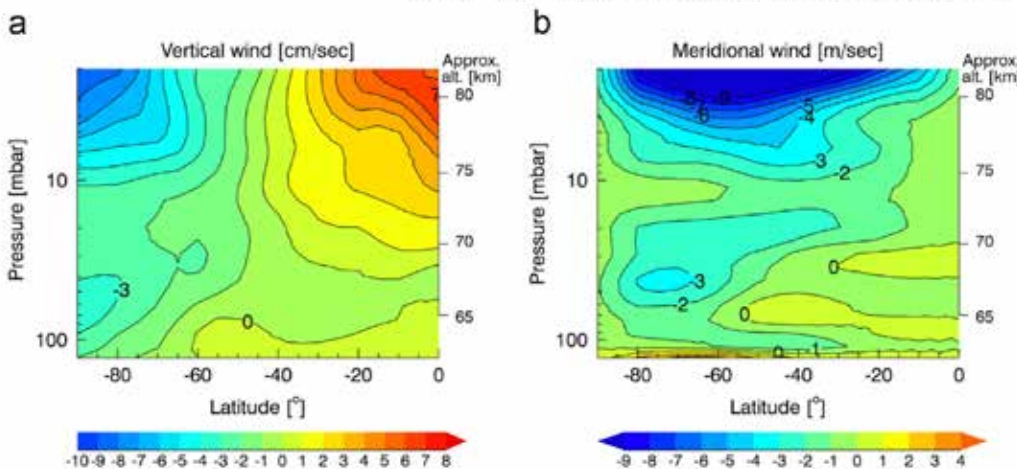


**Fig. 14.** Latitude–altitude field of the net radiative forcing in the Venus mesosphere. The temperature and cloud top structure are the same as in Figs. 9 and 13.



Ando et al. (2016)

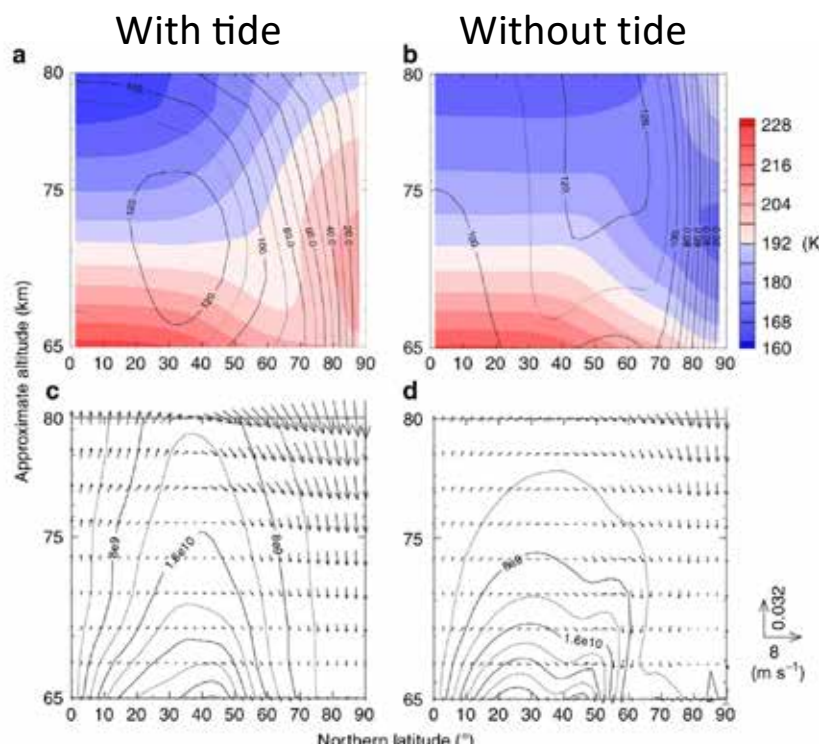
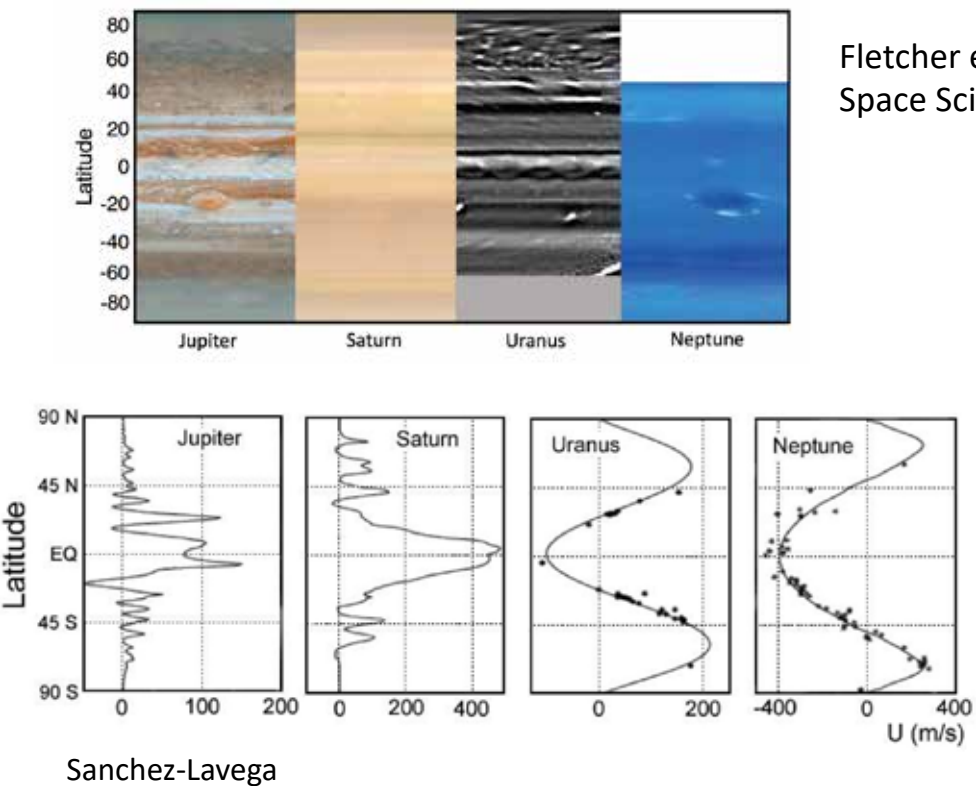
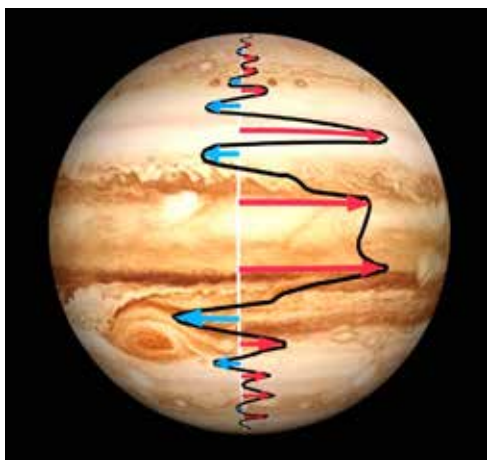


**Figure 6 | Meridional cross-sections of the zonally and temporally averaged zonal wind (solid line) and temperature (colour shade) and the horizontal and vertical components of the residual mean meridional circulation (vector) and mass stream function (contour). (a)** Zonal wind and temperature in Case A. **(b)** Those in Case B. **(c)** Residual mean meridional circulation vector and mass stream function in Case A. **(d)** Those in Case B. Averaged period is two Venusian solar days (234 Earth days) after settling into the quasi-steady state.

# Belt/zone circulation of giant planet atmospheres



## Winds on Jupiter



### Zones :

- Reflective white bands of low temperatures, and elevated aerosol opacities
- Anti-cyclonic vorticity

### Belts :

- Darker bands of warmer temperatures, and depleted aerosols
- Cyclonic vorticity

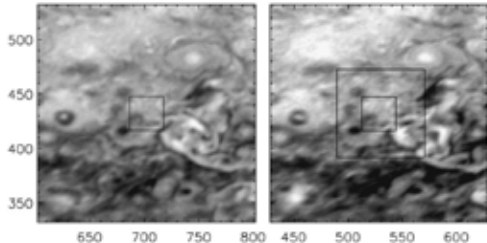


Cloud movie taken by Cassini spacecraft during its Jupiter flyby

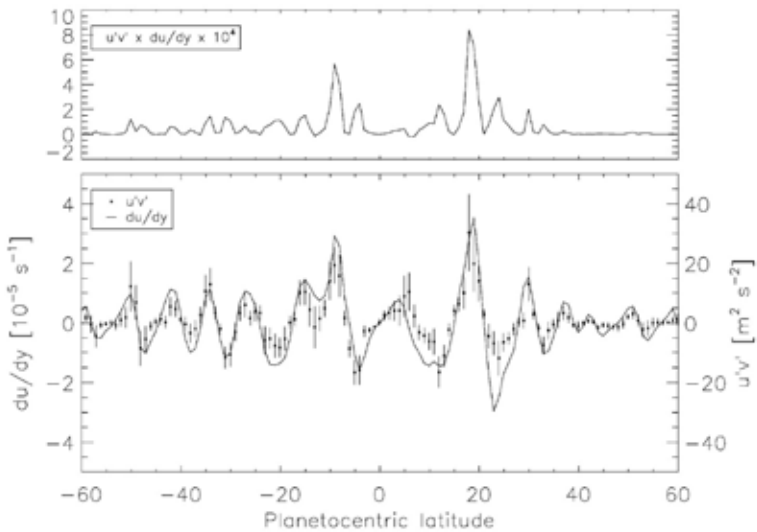
# Eddy momentum transport on Jupiter

Salyk et al. (2006)

Analysis of Cassini imaging data

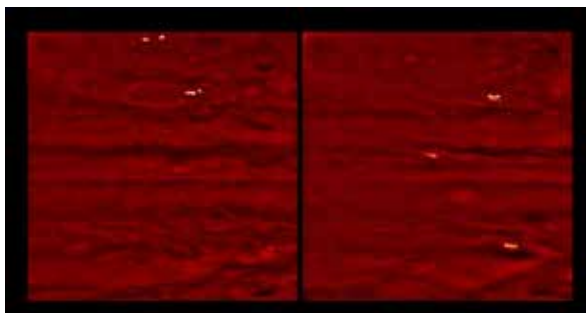


High positive correlation between eddy momentum flux,  $\langle u'v' \rangle$ , and the variation of zonal velocity with latitude,  $du/dy$ , was found.

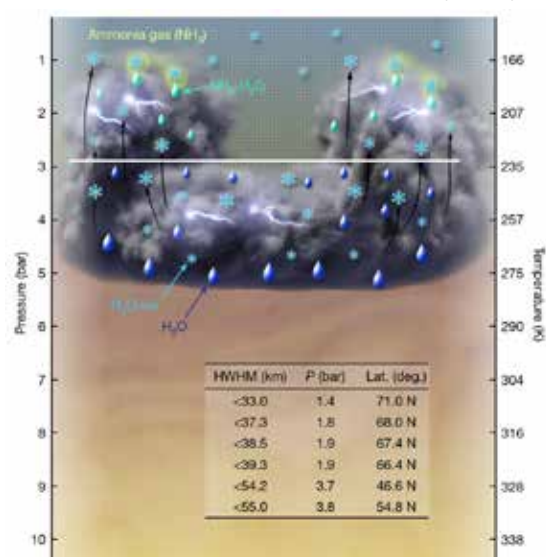


# Thunderstorms on Jupiter

Becker et al. (2020)



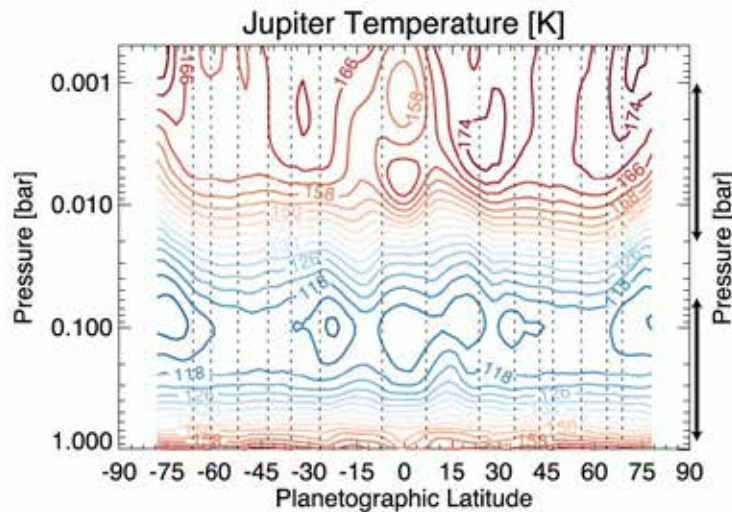
Lightning storms on the night side of Jupiter along with clouds dimly lit by moonlight from Io (taken by Galileo spacecraft)



On Jupiter, energy is transferred from the warm interior of the planet to the visible atmosphere to feed thunderstorms. Lightning occurs in the low-pressure regions.

Fig. 3 | Conceptual illustration of lightning generation above and below the 3-bar level in Jupiter's atmosphere. Energetic updraughts (black arrows) loft water-ice particles to altitudes between 1.1 and 1.5 bar, where adsorption of ammonia gas onto ice particles melts the ice, creating falling liquid ammonia-water ( $NH_3\text{-}H_2O$ ) particles (green drops). Charge separation occurs as the  $NH_3\text{-}H_2O$  particles collide with upward moving water-ice, followed by lightning. At pressures greater than about 3 bar, temperatures are above the limit for supercooled water (white line, about 233 K) and lightning is generated in pure water clouds. Inset, radial half-width at half-maximum (HWHM) intensity distances, estimated maximum depths of origin ( $P$ , pressure level) and latitudes (lat.) of observed SRU lightning flashes.

# Temperature field above the clouds of Jupiter retrieved from infrared observations



Vertical dotted lines : Prograde jets

Above clouds (upper-troposphere), the equatorward flanks of eastward jets (anticyclonic vorticity) are colder than the poleward flanks (cyclonic vorticity).

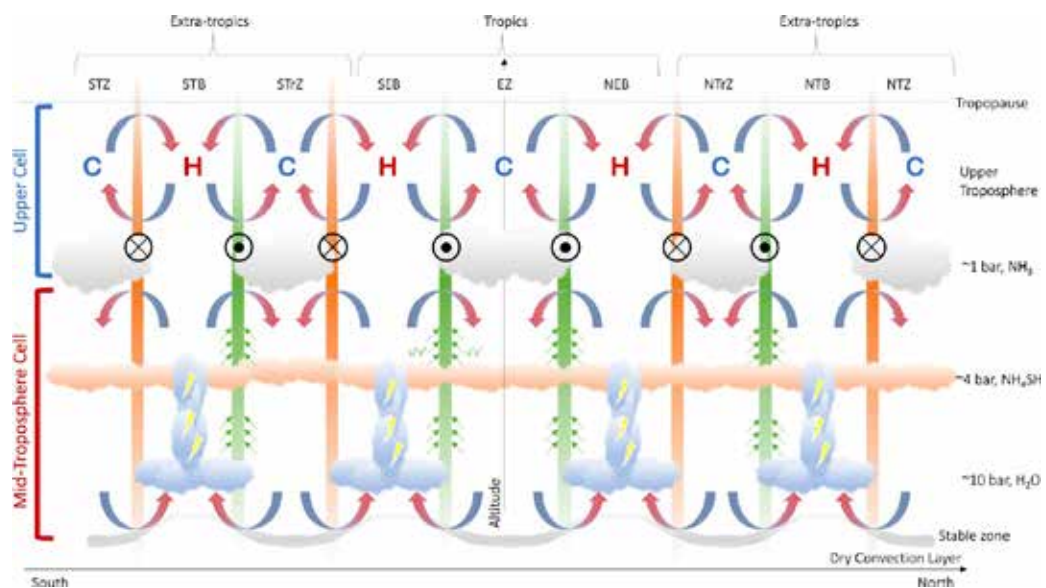
→ Thermal wind balance implies that the cloud-top winds decay with altitude.

$$\frac{\partial u_g}{\partial p} = \frac{R}{fp} \frac{\partial T}{\partial y}$$

Fletcher et al. (2020, Space Sci. Rev.)

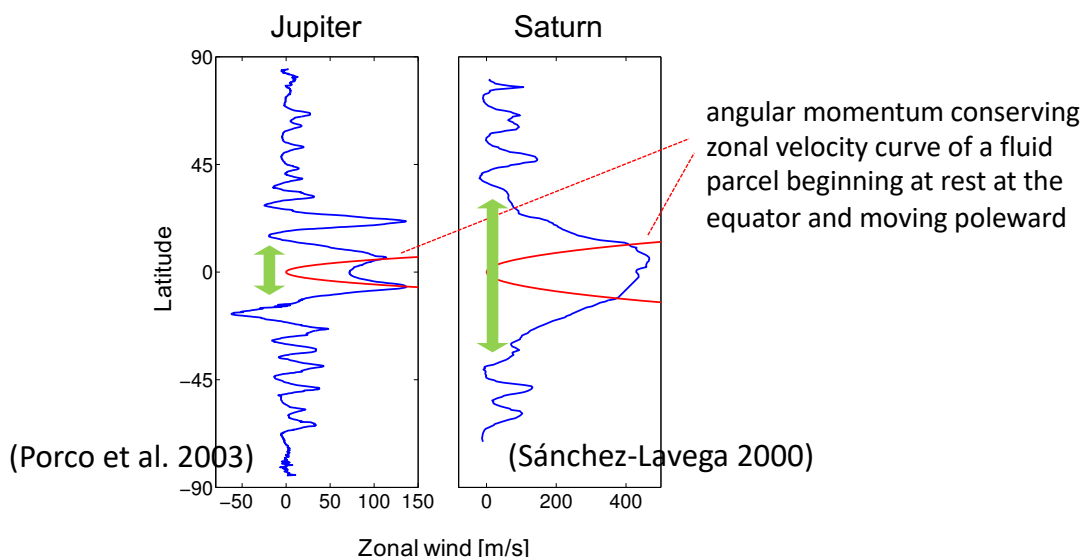
Fletcher et al. (2020, Space Sci. Rev.)

Upwelling in zones inferred from the upper tropospheric temperature structure, which implies decay and dissipation of the zonal jets with altitude above the clouds



Upwelling in belts inferred from the convergence of eddy angular momentum into the eastward zonal jets at the cloud level

# Superrotation on the gas giants

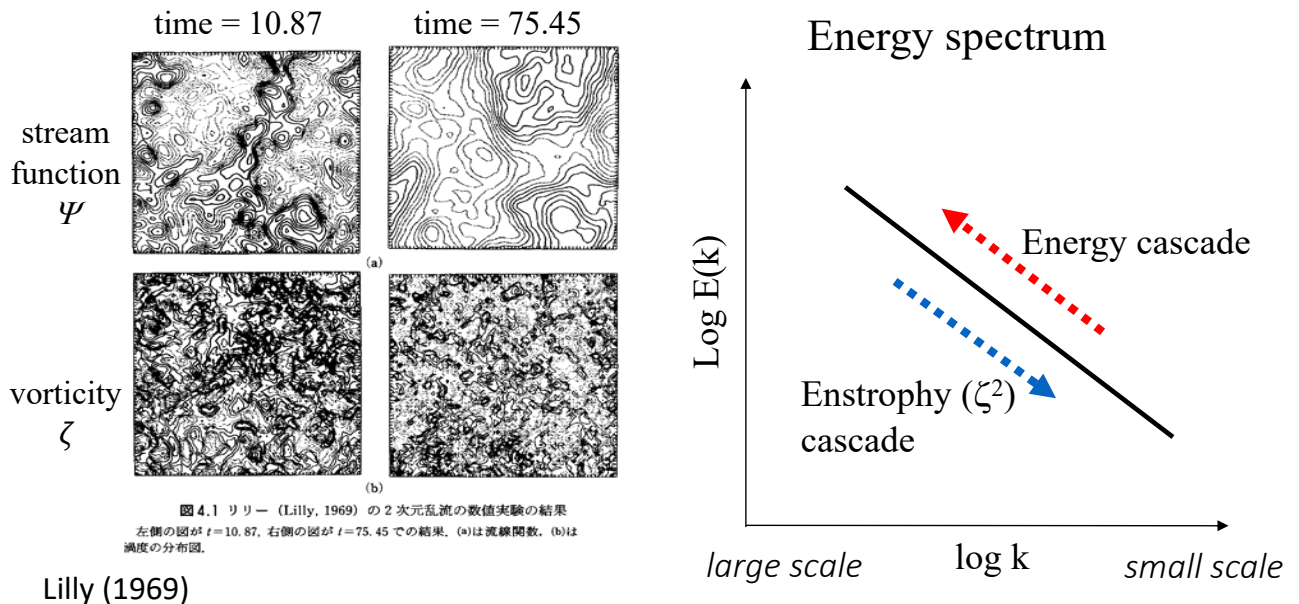


## Modeling Jupiter and Saturn's zonal flows

- Shallow models
  - The dynamics are shallow, such as on a terrestrial planet
  - The strong east-west flows can result from 2D geostrophic turbulence and/or baroclinic instability
- Deep models
  - the observed jets are the surface manifestation of convective columns originating from the hot interiors

# Two-dimensional turbulence

- Small eddies tend to organize large eddies as time passes
- Turbulent energy cascade toward large scales (smaller wavenumber  $k$ )



## Rhines scale

- Vorticity equation

$$\left( \frac{\partial}{\partial t} + \vec{v}_g \cdot \nabla \right) (\zeta_g + f) = 0$$

$$\frac{\partial \zeta}{\partial t} + u \frac{\partial \zeta}{\partial x} + v \frac{\partial \zeta}{\partial y} + \beta v = 0$$

nonlinear term	beta effect
= origin of	= origin of
turbulence	Rossby wave

→  $k^2 U^2 > \beta U$  : turbulence       $\beta : df/dy$   
 $k^2 U^2 < \beta U$  : Rossby wave       $U : \text{typical velocity}$

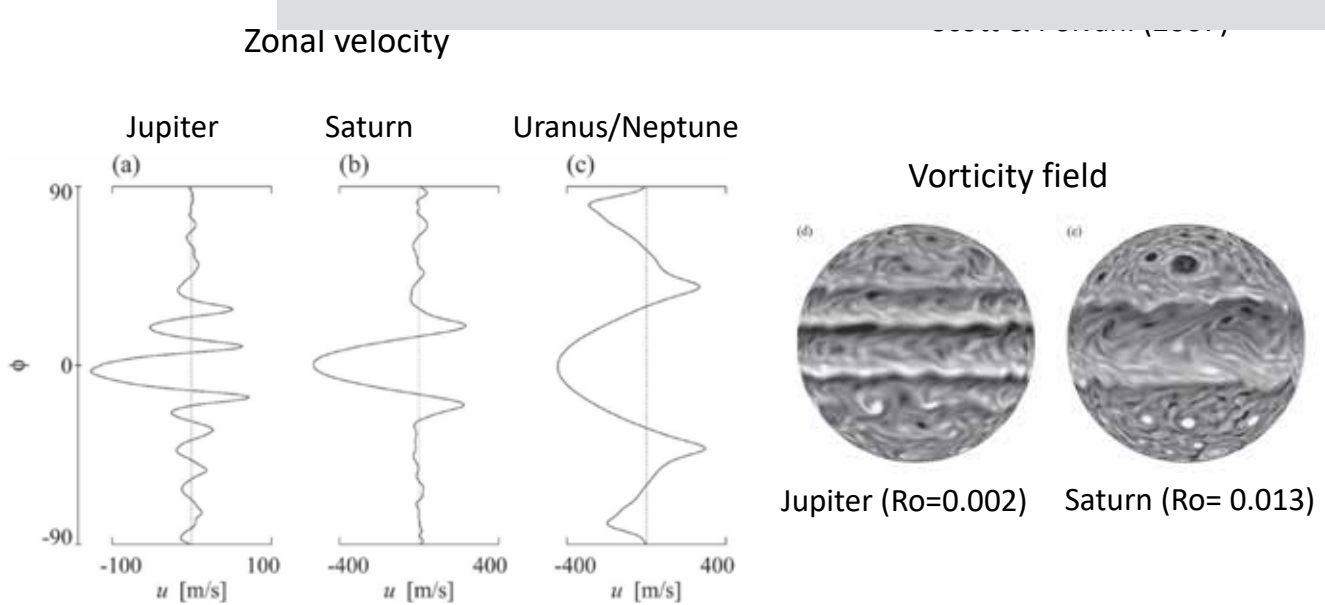
- Rhines scale

$$k_\beta = \sqrt{\frac{\beta}{U}}$$

Upward cascade of turbulence energy stops at smaller scales ( $k < k_\beta$ )

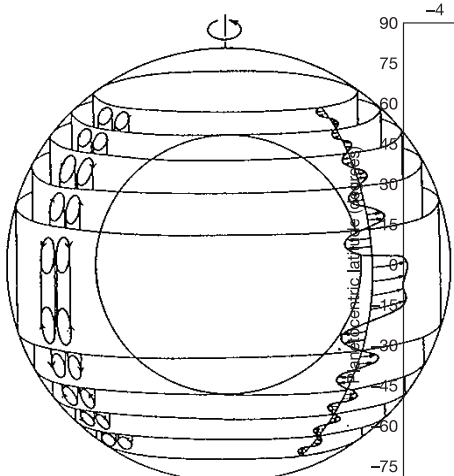
# Shallow-water turbulence on the sphere of the giant planets

- Forcing are given to the vorticity field as a small-scale, random process, or eddies are generated by baroclinic instability
- Inverse energy cascade generates multiple jets on the order of the Rhines scale
- The simulated equatorial flow is mostly retrograde



## Deep models: Taylor–Proudman theorem

- In a fluid that is steadily rotated, the fluid velocity will be uniform along any line parallel to the axis of rotation.



Momentum equation in rotational frame

$$\frac{d\vec{v}}{dt} + 2\vec{\Omega} \times \vec{v} + \frac{1}{\rho} \nabla p + \nabla \Phi = 0$$

Assuming non-compressibility and  $d/dt=0$ , the curl is applied to give

$$\vec{\Omega} \cdot \nabla \vec{v} = 0$$

Taking z-axis along the planet's rotational axis,

$$\frac{\partial \vec{v}}{\partial z} = 0$$

Busse (1994)

# Quasi-geostrophic vorticity equation

$$\frac{\partial \zeta_g}{\partial t} = -\vec{v}_g \cdot \nabla(\zeta_g + f) + f_0 \frac{\partial \omega}{\partial p}$$

$$\zeta_g = \frac{\partial v_g}{\partial x} - \frac{\partial u_g}{\partial y} = \frac{\nabla^2 \Phi'}{f_0} \quad : \text{geostrophic vorticity}$$

Vorticity changes with time through

- advection of absolute vorticity ( $\zeta_g + f$ ) by geostrophic wind ( $\vec{v}_g$ )
- vertical divergence (horizontal divergence)

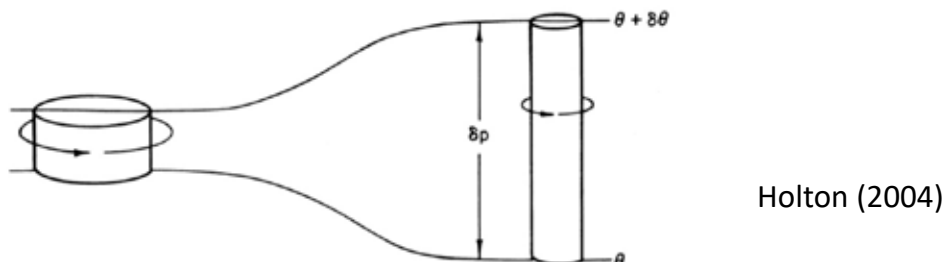


Fig. 4.7 A cylindrical column of air moving adiabatically, conserving potential vorticity.

## Thermal Rossby wave

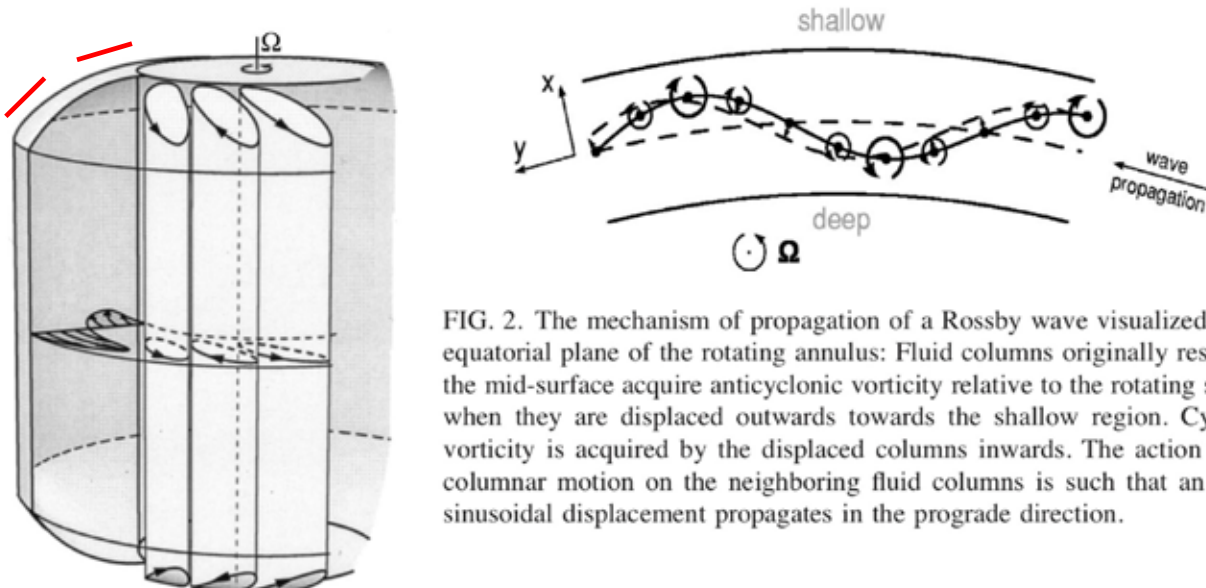
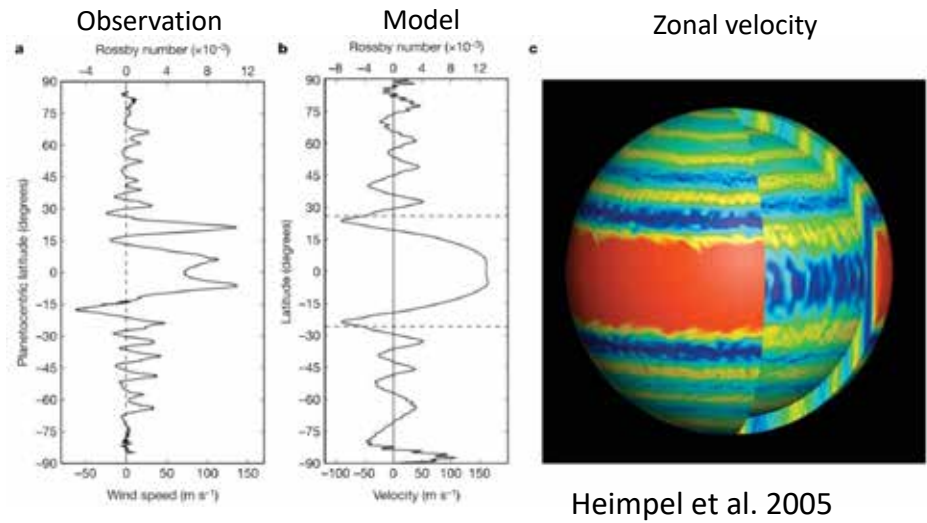


FIG. 2. The mechanism of propagation of a Rossby wave visualized in the equatorial plane of the rotating annulus: Fluid columns originally resting at the mid-surface acquire anticyclonic vorticity relative to the rotating system when they are displaced outwards towards the shallow region. Cyclonic vorticity is acquired by the displaced columns inwards. The action of the columnar motion on the neighboring fluid columns is such that an initial sinusoidal displacement propagates in the prograde direction.

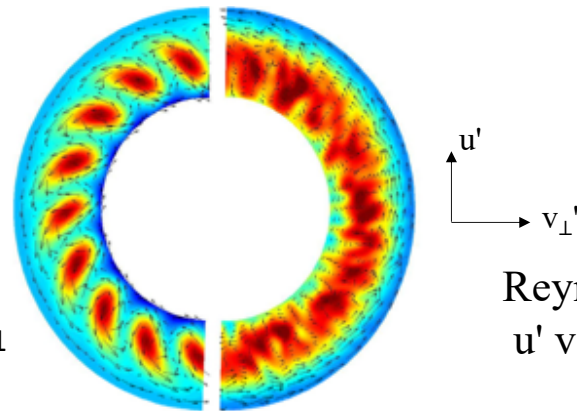
Busse (2002)

The columns are tilted because the thermal Rossby wave has the tendency to propagate faster on the outside than on the inside. A prograde differential rotation on the outside with a retrograde one near the inner cylinder must thus be expected.

# Deep models



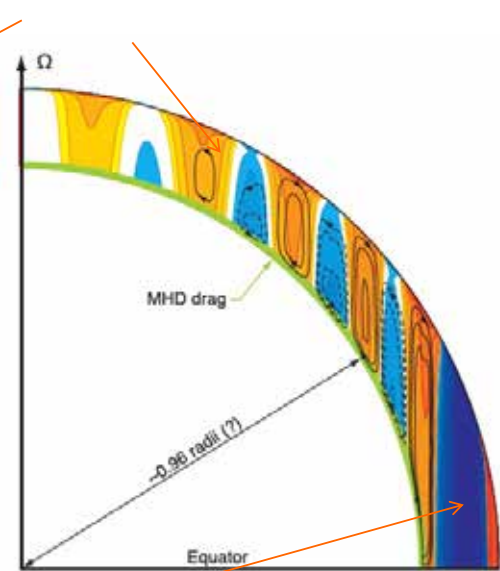
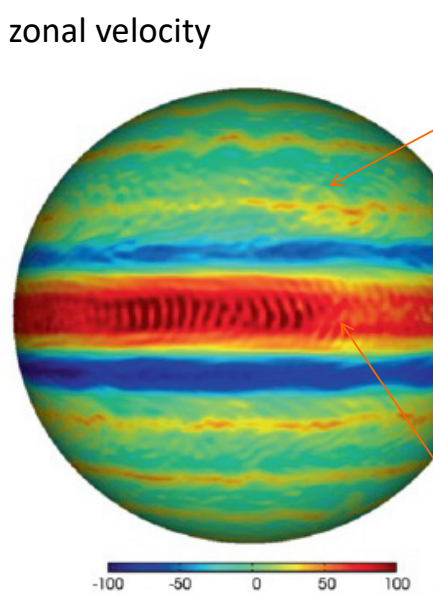
Showman et al. 2011



## Modeling of Jupiter

Schneider & Liu, 2009

baroclinic eddies generated by differential radiative heating are responsible for Jupiter's off-equatorial jets



Rossby waves generated by intrinsic convective heat fluxes are responsible for the equatorial superrotation

# Doppler tracking of Juno spacecraft

Less et al. (2018)

- The spacecraft acts as a test particle falling in the gravity field of the planet. Jupiter's gravity is inferred from range-rate measurements between a ground antenna and the spacecraft during perijove passes.
- The ground station transmits carrier signals, and the on-board translator lock the incoming carrier signals and retransmit them back to the ground. The range-rate (Doppler) observable is obtained by comparing the transmitted and received frequencies.
- Spherical harmonics representation of planetary gravity fields is determined by the density distribution inside the body.

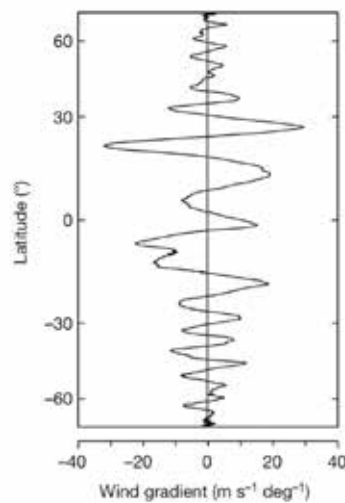
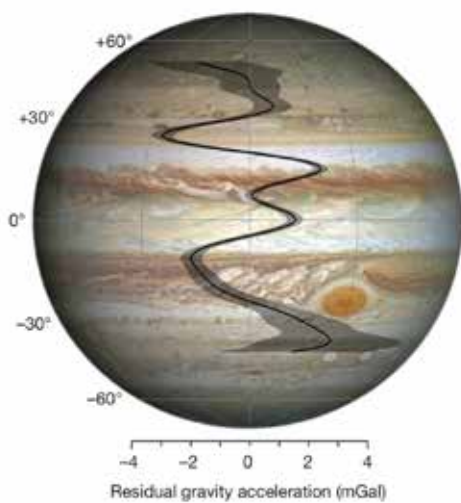
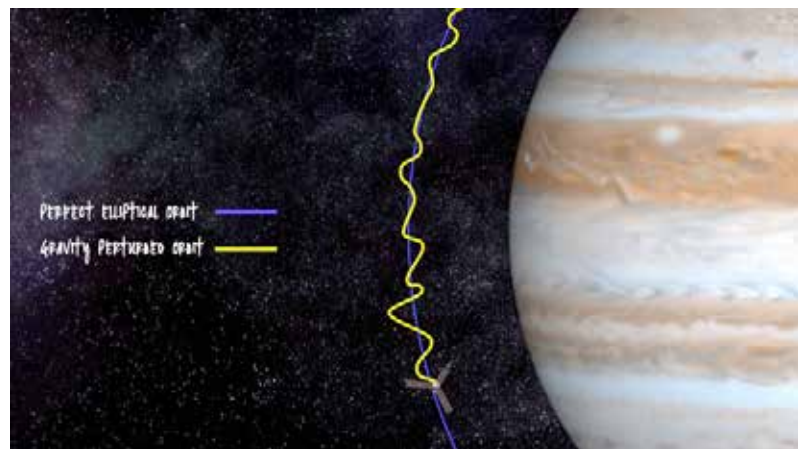
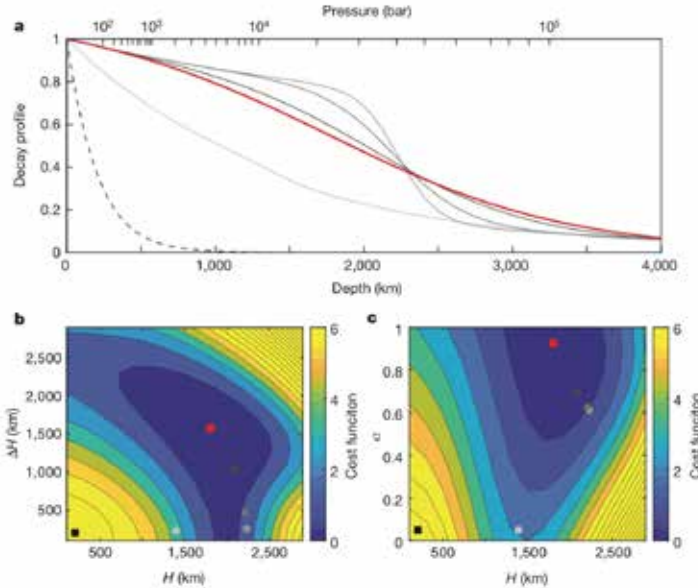
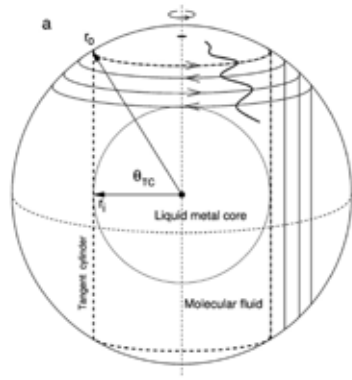


**Figure 3 | Gravity disturbances due to atmospheric dynamics.** a, An image of Jupiter taken by the Hubble Wide Field Camera in 2014 (<https://en.wikipedia.org/wiki/Jupiter>), showing the latitudinal dependence of residual gravity acceleration (in milligals, positive outwards) and associated  $3\sigma$  uncertainty (shaded area) at a reference distance of 71,492 km, when the gravity from the even zonal harmonics  $J_2$ ,  $J_4$ ,  $J_6$  and  $J_8$  is removed. The residual gravity field, which is dominated by the dynamics of the flows, shows marked peaks correlated with the band structure. b, Latitudinal gradient of the measured wind profile. The largest (negative) peak of  $-3.4 \pm 0.4$  mGal ( $3\sigma$ ) is found at a latitude of  $24^\circ$  N, where the latitudinal gradient of the wind speed reaches its largest value. The relation between the gravity disturbances and wind gradients is discussed in an accompanying paper<sup>4</sup>.

Less et al. (2018)



$$u(r, \theta) = u_{\text{cyl}}(s)Q(r) \quad (12)$$

where  $u_{\text{cyl}}(s)$  is the cloud-level azimuthal wind projected downward along the direction of the axis of rotation, and  $s = r\cos(\theta)$  is the distance from the axis of rotation.  $Q(r)$  is the radial decay function we optimize, given by

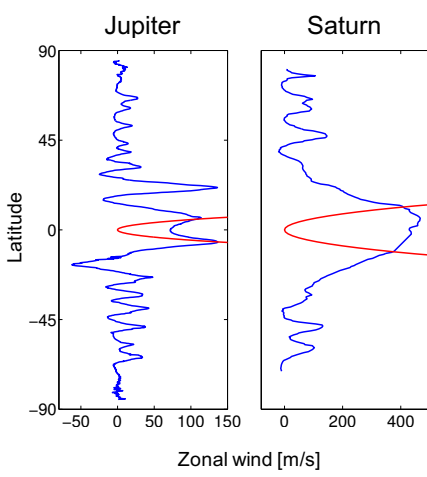
$$Q(r) = (1 - \alpha)\exp\left(\frac{r-a}{H(\theta)}\right) + \alpha \left[ \frac{\tanh\left(-\frac{a-H(\theta)-r}{\Delta H}\right) + 1}{\tanh\left(\frac{H(\theta)}{\Delta H}\right) + 1} \right] \quad (13)$$

where  $a$  is the planetary radius,  $\alpha$  is the contribution ratio between an exponential and a normalized hyperbolic tangent function and  $\Delta H$  is the width of the hyperbolic tangent. We take a hierachal approach using this profile at several levels of

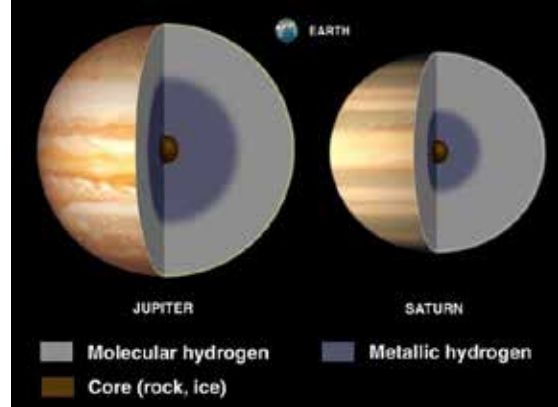
Kaspi et al. (2018)

The observed jet streams, as they appear at the cloud level, extend down to depths of thousands of kilometres beneath the cloud level, probably to the region of magnetic dissipation at a depth of about 3,000 kilometres

## Difference between Jupiter and Saturn



(Porco et al. 2003) (Sánchez-Lavega 2000)

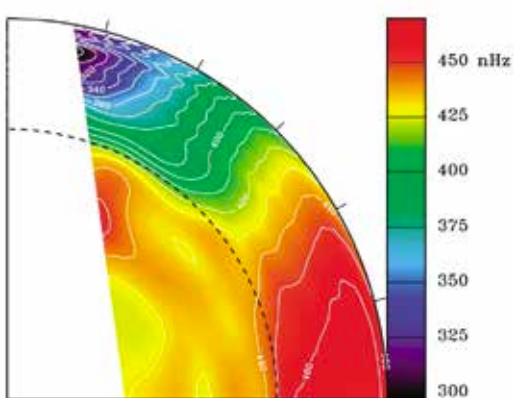


from Wikipedia

- JunoとCassiniの重力計測によれば土星のジェットは木星に比べて3倍の深さまで及んでいる(木星:3000 km vs. 土星:9000 km). これは大気が導電性を持ちオーム抵抗が生じる深さに対応すると考えられる。
- 赤道スーパーローテーションの到達緯度は木星では  $13^\circ$ 、土星で  $31^\circ$  くらい。これは導電性が生じる深さから自転軸方向に伸ばした直線が表面と交わるあたりに相当する。

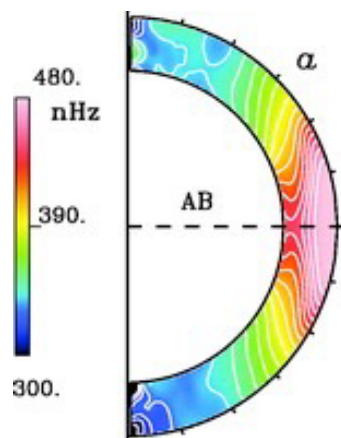
# Equatorial superrotation in the Sun

Rotation rates revealed by  
helioseismology

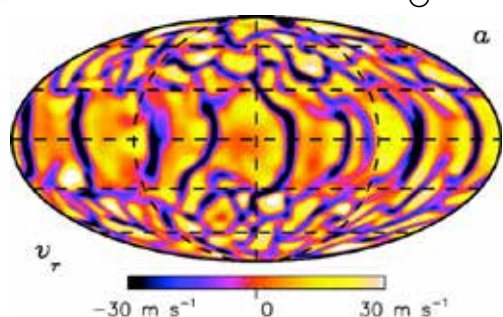


Rot. rate = 25 days on the equator  
36 days near the poles

Numerical modeling (Miesch 2000)



Vertical velocity  
at  $r = 0.95 R_\odot$



Equatorward angular momentum  
transport by slant convection ?